Impact of ocean heat transport on sea ice captured by a simple energy balance model

Aylmer, J. R. ORCID: https://orcid.org/0000-0002-5159-0608, Ferreira, D. ORCID: https://orcid.org/0000-0003-3243-9774 and Feltham, D. L. ORCID: https://orcid.org/0000-0003-2289-014X (2024) Impact of ocean heat transport on sea ice captured by a simple energy balance model. Communications Earth & Environment, 5. 406. ISSN 2662-4435 doi: https://doi.org/10.1038/s43247-024-01565-7 Available at https://centaur.reading.ac.uk/117331/

It is advisable to refer to the publisher's version if you intend to cite from the work. See [Guidance on citing](#).

To link to this article DOI: http://dx.doi.org/10.1038/s43247-024-01565-7

www.reading.ac.uk/centaur

CentAUR

Central Archive at the University of Reading

Reading's research outputs online

Impact of ocean heat transport on sea ice captured by a simple energy balance model

Check for updates

Jake R. Aylmer [1,2] ✉, David Ferreira [1,3] & Daniel L. Feltham[1,2,3]

Future projections of Arctic and Antarctic sea ice suffer from uncertainties largely associated with inter-model spread. Ocean heat transport has been hypothesised as a source of this uncertainty, based on correlations with sea ice extent across climate models. However, a physical explanation of what sets the sea ice sensitivity to ocean heat transport remains to be uncovered. Here, we derive a simple equation using an idealised energy-balance model that captures the emergent relationship between ocean heat transport and sea ice in climate models. Inter-model spread of Arctic sea ice loss depends strongly on the spread in ocean heat transport, with a sensitivity set by compensation of atmospheric heat transport and radiative feedbacks. Southern Ocean heat transport exhibits a comparatively weak relationship with Antarctic sea ice and plays a passive role secondary to atmospheric heat transport. Our results suggest that addressing ocean model biases will substantially reduce uncertainty in projections of Arctic sea ice.

Reduction of Arctic sea ice in recent decades is a striking and widely-publicised indicator of climate change[1,2]. Sea ice plays a major role in shaping the Arctic environment, and its ongoing transformation affects trade, bio-diversity, and indigenous populations[3–7]. Models project further sea ice decline throughout the twenty-first century[8], amplifying such impacts and global climate change itself[9,10] via large-scale feedback loops[11–15]. At the opposite pole, Antarctic sea ice has not exhibited such a clear connection with global warming, with strong interannual variability and opposing regional trends presenting a substantial challenge to simulations[16,17]. For several generations of the Coupled Model Intercomparison Project (CMIP), projections of future Arctic and Antarctic sea ice have suffered from large uncertainties, arising in part from inter-model spread[8,17–24]. Furthermore, models underestimate the observed Arctic sea ice sensitivity to global warming[8,25] and fail to reproduce pan-Antarctic sea ice expansion prior to 2016[16,17]. These uncertainties harm confidence in our ability to robustly simulate the large-scale climate and quantify the impacts of different environmental policies[15,24,26,27].

Previous literature strongly points to ocean heat transport (OHT) as a major driver of sea ice in both hemispheres on multidecadal timescales. When general circulation models (GCMs) simulate greater OHT into the polar regions, their sea ice area tends to be smaller, as found in a variety of study designs ranging from idealised experiments to coupled runs with realistic greenhouse gas forcing[28–38]. This relationship in models is supported by observations, despite limited temporal availability. In-situ current and temperature measurements reveal increasing OHT into the Barents Sea in recent years correlated with local sea ice extent[37,39]. Sea ice loss in that region is driving increased sensitivity to Atlantic OHT, through weakening of the Arctic Ocean stratification favouring ocean heat release[40]. Under Antarctic sea ice, reduced ocean–ice heat flux has been proposed as an explanation for its increasing trend before 2016[41–43]. Strong inter-model correlations between OHT and sea ice have raised the hypothesis that ocean biases could explain a substantial fraction of model spread in sea ice[44–48]. Such correlations are intuitive but previous studies have been unable to explain their origin; specifically, what sets the rate of sea ice loss per OHT change, i.e., sensitivity, among different models? This relationship suggests that OHT contributes to the relative differences in the amount of sea ice loss across models, hence inter-model spread, and is the focus of the present work. Note that this is distinguished from quantifying how much sea ice loss occurs due to OHT in a given simulation, the multi-model mean, or reality, for which it may or may not be more important than atmospheric forcing[49,50]. In other words, we examine the role of OHT in setting differences in the trends, not the trends themselves.

Zonal-average energy-balance models (EBMs) combine simple expressions of vertical and latitudinal heat exchange to describe the large-scale climate. Originally developed to examine the ice albedo feedback before widespread use of GCMs[51–55], they remain powerful tools that have been adapted to modern, conceptual studies of sea ice stability and drivers[56–64], and used to interpret GCM behaviour in a variety of

[1]Department of Meteorology, University of Reading, Reading, Berkshire, RG6 6ET, UK. [2]Centre for Polar Observation and Modelling (CPOM), Department of Meteorology, University of Reading, Reading, Berkshire, RG6 6ET, UK. [3]These authors contributed equally: David Ferreira, Daniel L. Feltham. ✉e-mail: j.aylmer@reading.ac.uk

contexts[65–73]. Here, we use EBM principles to show how the emergent sensitivity of sea ice to OHT arises from constraints on energy conservation, revealing the underlying atmospheric processes that explain and set its magnitude. This provides, for the first time, a theoretical grounding for the extensively-documented correlation between sea ice and OHT, implying a profound role of OHT in offsetting or enhancing simulated Arctic sea ice loss under global warming. This is confirmed when extending our analysis to mid twenty-first century projections. In the Southern Ocean, changes in Antarctic sea ice are related to OHT more weakly than in the Arctic and a more nuanced picture emerges suggesting it plays a passive role, with less multi-model consistency compared to the Arctic.

Results

Simulating historical Arctic changes

We start by examining Arctic sea ice and polar surface temperature changes over recent decades in CMIP6 simulations. These are quantified using the zonal-mean latitude of the sea ice edge, ϕ_i, and the mean near-surface temperature, T, poleward of a reference latitude, $\phi_0 = 65°N$ (see Methods). Changes are computed as the difference in means between the two time periods 2001–2021 and 1980–2000, to capture multidecadal variability and maximise overlap with the observational record. This data is plotted in Fig. 1a for a total of 105 simulations from 20 models (Table 1), which shows a strong positive correlation ($r = 0.97$) between the simulated warming and sea ice-edge retreat (positive $\Delta\phi_i$), and an effective sensitivity of about 1.4°N K^{-1}. We compare with the observed ice-edge change and its uncertainty derived from satellite retrievals of sea ice concentration, shown by the vertical bars in Fig. 1a (see Methods). The range of $\Delta\phi_i$ in models (about 5°N) is about six times larger than observational uncertainty (0.85°N) in the northern hemisphere, illustrating substantial spread in the rates of Arctic sea ice loss in models. All but one simulation exhibit mean sea ice retreat. Figure 1a also shows real-world polar temperature change as estimated from four modern atmospheric reanalyses.

Thirteen percent of simulations lie strictly within the uncertainty limits of our estimates of the real-world Arctic sea ice and surface temperature changes. The range of simulated changes in Arctic sea ice edge is roughly centred on observations, perhaps reflecting the use of Arctic sea ice as a tuning metric[74–76]. There is no conspicuous offset of the group of model points relative to

observations, unlike the analogous plot with global-mean surface temperature (GMST) rise[8,25]. With GMST, there is reduced (but still significant) correlation with Arctic sea ice change, and an offset such that realistic sea ice trends are associated with too fast global warming (Supplementary Fig. 1a).

Next, we add the change in poleward OHT across the reference latitude within which T is averaged (see Methods). Simulations exhibiting larger (smaller) increases in OHT towards the Arctic tend to overestimate (underestimate) both sea ice loss and polar warming (Fig. 1b), corresponding to an emergent sensitivity in which 1°N change in ice edge occurs with a change in OHT of about 30 TW. The relationship between ΔOHT and $\Delta\phi_i$ is roughly linear, but less correlated ($r = 0.83$) than the relationship between ΔT and $\Delta\phi_i$ ($r = 0.97$; i.e., more scatter; cf. Fig. 1a, b). About 20% of simulations simulate decreasing OHT in the Arctic, while the sea ice and surface temperature changes are almost all positive. This is consistent with previous studies on the drivers of Arctic sea ice loss in model simulations which are divided roughly equally on the main driver—OHT or atmospheric warming—of sea ice decline[50]. Simulations with small changes in OHT tend to get closest to the observed sea ice change, although there is non-negligible scatter with higher estimates of $\Delta\phi_i$ occurring with higher ΔT. Ocean heat transport data diagnosed from the latest ECCO (Estimating the Circulation and Climate of the Ocean) product, the horizontal bar on Fig. 1b, shows a small increase but is indistinguishable from zero. Caution should be taken with this estimate as it is based on 1992–2019 data, hence the first time averaging period being less than half covered by the data (see Methods for how we calculate the corresponding uncertainty range). Still, it suggests that simulations tend to exhibit the most realistic Arctic sea ice retreat when the OHT is also realistically simulated.

We have thus far considered the relationships between sea ice and surface temperature and between sea ice and OHT over the historical period. In the next section, we present our EBM approach that shows how all three quantities are co-related, and examine the extent to which the CMIP6 ensemble conform to this theory.

Energy balance model

Conservation of energy dictates that changes in the polar top-of-atmosphere (TOA) fluxes, namely the net shortwave and outgoing longwave radiation (OLR), must be balanced by a change in the net heat transport across ϕ_0
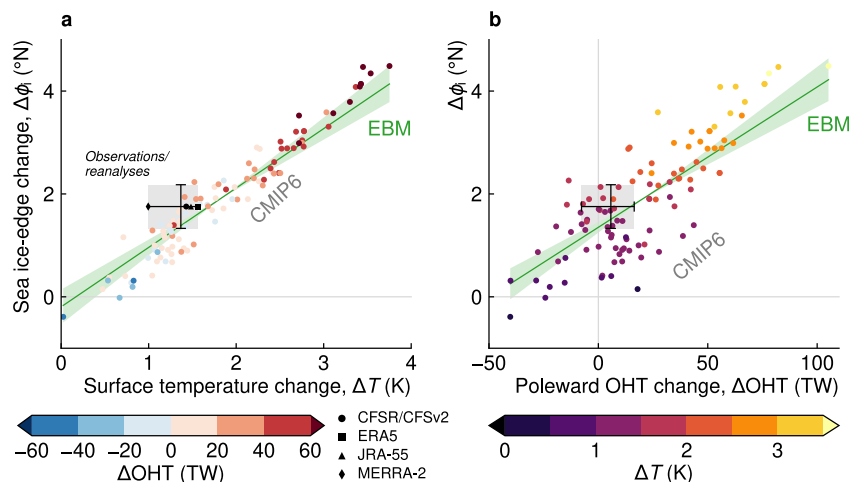

Fig. 1 | Arctic sea ice, polar temperature, and ocean heat transport changes over 1980–2021. a Change in mean Arctic sea ice-edge latitude, $\Delta\phi_i$, plotted against change in polar (latitudes poleward of 65°N) near-surface air temperature, ΔT, in CMIP6 simulations. Changes are computed as the difference in the 21 year means over 2000–2021 and over 1980–2000. Each point is an individual simulation, and its colour (blue–red scale) indicates the change in poleward ocean heat transport (ΔOHT; across 65°N, in units of 1 TW = 10^{12} W) between the same time periods. Estimates of the corresponding real-world changes are indicated by the vertical bar (uncertainty range derived from satellite observations of sea ice concentration) and

horizontal bar (different atmospheric reanalyses indicated by black symbols; see Methods). The energy-balance model (EBM) estimate of the sensitivity using Eq. (1) is shown by the green lines and shading (standard error propagated from underlying parameters), which is plotted through the ensemble mean. **b** As in (**a**) but with the OHT and temperature data switched, so that the former is plotted on the horizontal axis and the latter is shown by the colour (purple–yellow) scale. The horizontal bar represents an estimate of the real-world OHT change over this time period from the Estimating the Circulation and Climate of the Ocean (ECCO) ocean state estimate (see Methods).

Table 1 | List of CMIP6 models analysed and relevant metadata

Model	t_{PI}	ϕ_i	OHT	Ensemble members	
AWI-CM-1-1-MR[129–132]	500	0.25°	residual	5	r(1–5)i1p1f1
CESM2[133–136]	1200	0.5°	residual	3	r(4,10–11)i1p1f1
CESM2-FV2[133,137–139]	150	1°	residual	1	r1i2p2f1
CESM2-WACCM[133,140–142]	500	0.5°	residual	1	r1i1p1f1
CNRM-CM6-1[106,143,144]	—	1°	hfx/hfy	6	r(1–6)i1p1f2
CNRM-CM6-1-HR[106,145–147]	300	0.25°	hfx/hfy	1	r1i1p1f2
CNRM-ESM2-1[107,148,149]	—	1°	hfx/hfy	1	r1i1p1f2
CanESM5[150–153]	1051	1°	residual	25	r(1–25)i1p2f1
CanESM5-CanOE[150,154–156]	500	1°	residual	3	r(1–3)i1p2f1
GFDL-ESM4[157–160]	500	1°	hfbasin	1	r1i1p1f1
GISS-E2-2-G[161–164]	296	2°	hfbasin	5	r(1–5)i1p3f1
IPSL-CM6A-LR[165–168]	1000	1°	residual	11	r(1–10,14)i1p1f1
MIROC6[169–172]	800	1°	hfbasin	1	r1i1p1f1
MPI-ESM1-2-HR[173–176]	500	0.5°	residual	10	r(1–10)i1p1f1
MPI-ESM1-2-LR[177–180]	1000	1°	residual	10	r(1–10)i1p1f1
MRI-ESM2-0[181–184]	700	0.5°	hfbasin	5	r(1–5)i1p1f1
NorESM2-LM[185–188]	501	1°	hfbasin	1	r1i1p1f1
NorESM2-MM[185,189–191]	500	1°	hfbasin	1	r1i1p1f1
UKESM1-0-LL[108,192–194]	1880	1°	hfx/hfy	13	r(1–4,8–12,16–19)i1p1f2
UKESM1-1-LL[108,195–197]	462	1°	hfbasin	1	r1i1p1f2

From left to right: Model name as listed in the CMIP6 archive; length in years of its pre-industrial control simulation, t_{PI}, if available; regular grid resolution that sea ice concentration is interpolated to before calculation of the ice edge latitude, ϕ_i; method by which ocean heat transport (OHT) is computed (see Methods); number and identities of the ensemble members analysed (historical and SSP3-7.0 simulations). Ensemble members are identified by the (r) realisation, (i) initialisation, (p) physics, and (f) forcing indices.

(Fig. 2). Drawing from the EBM literature[57,61,62], we have derived (see Methods) a simple equation relating changes in the sea ice-edge latitude, $\Delta\phi_i$, polar surface temperature, ΔT, and ΔOHT, of the form:

$$S\Delta\phi_i = R\Delta T - C\Delta\text{OHT}. \qquad (1)$$

Equation (1) is essentially a rearranged expression for the TOA energy balance. Sea ice appears because it can be related to the shortwave radiation via its influence on the planetary albedo[14]; the coefficient S accounts for this and is treated as a constant (and derived independently using pre-industrial control simulation data; see Methods). The surface temperature change appears because of its linear relationship to surface fluxes and OLR[62,77,78]. Radiative feedbacks at the surface and TOA are combined into the coefficient R which, like S, is treated as a constant. Changes in atmospheric heat transport (AHT) and the rate of ocean heat uptake are accounted for, completing the energy budget—these depend strongly on OHT and are represented as correction factors in the coefficient C of ΔOHT. It should be emphasised that the three variables, $\Delta\phi_i$, ΔT, and ΔOHT, in Eq. (1) are not independent; they represent net changes as a result of an arbitrary climate adjustment and each pair thus has covariance. For example, it is not possible to simply read off the relative impacts of OHT and T on ϕ_i from the coefficients in Eq. (1), hence the non-intuitive minus sign of the second term.

The details of S, R, and C, and an explicit derivation of Eq. (1) are given in Methods, but the role of AHT is worth highlighting here. Bjerknes compensation refers to the tendency of AHT to decrease when OHT increases[79]. This behaviour widely occurs in climate models[80–83], and we have exploited it to express ΔAHT as a function of ΔOHT, building this into the parameter C in Eq. (1). Due to Bjerknes compensation, correlations between ΔAHT and $\Delta\phi_i$ or ΔT are counterintuitive: simulations with larger increases in AHT tend to have cooler Arctic regions with less sea ice loss because of the corresponding larger decreases in OHT.

Dividing Eq. (1) through by $S\Delta$OHT gives an expression for the sea ice sensitivity to OHT—i.e., theoretical values of the slope of data in Fig. 1b, shown there by the green line (see Methods for the details of these
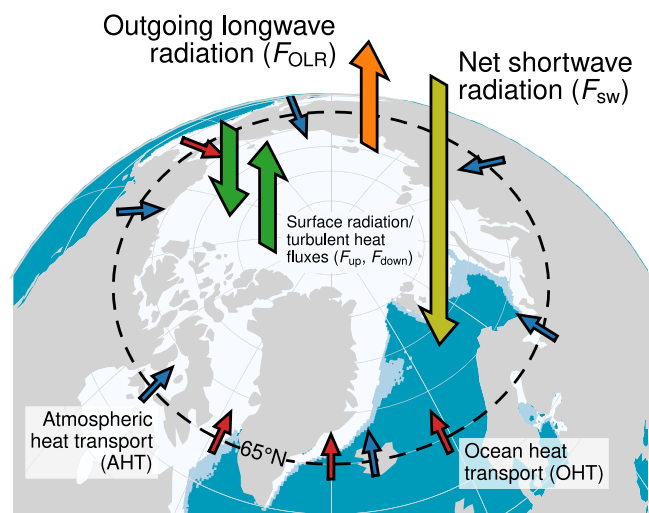

Outgoing longwave radiation (F_{OLR})

Net shortwave radiation (F_{sw})

Surface radiation/turbulent heat fluxes (F_{up}, F_{down})

Atmospheric heat transport (AHT)

65°N

Ocean heat transport (OHT)

Fig. 2 | Large-scale energy budget of the Arctic system. Our energy-balance model considers the north-polar cap at 65°N, i.e., the poleward region enclosed by the black dashed line. The ocean (OHT, red arrows) and atmosphere (AHT, blue arrows) transport heat across the boundary at 65°N into the domain. Changes in these quantities are balanced by top-of-atmosphere outgoing longwave radiation (F_{OLR}, orange arrow) and net shortwave radiation (F_{sw}, yellow arrow). Internally, surface fluxes of longwave radiation and sensible and latent heat (F_{up} and F_{down}, green arrows; see Methods) exchange heat between the atmosphere, ocean, and sea ice. Vertical heat fluxes are averages over the whole cap, and the AHT and OHT are integrated zonally at 65°N. The white area is the annual mean sea ice extent from observations averaged over 2001–2021, and the pale-blue areas are that for the period 1980–2000.

calculations). We could equally rearrange Eq. (1) for the sea ice sensitivity to surface temperature (dividing it through by $S\Delta T$), giving estimates of the slopes in Fig. 1a. Both ways closely capture the aggregate, multi-model relationship between historical changes in Arctic sea ice, polar surface temperature, and OHT. The EBM thus explains climate model spread in projected sea ice loss in terms of large-scale energetic constraints as quantified by Eq. (1). More specifically, it shows that the relationship between sea ice and OHT arises as a consequence of these constraints, some of which, notably, are not climate-change dependent (i.e., S and R being derived from pre-industrial data).

Is OHT a driver or consequence of sea ice loss?

The EBM Eq. (1) alone cannot be used to infer causality. Increased OHT driving additional reduction in sea ice cover is clearly a plausible interpretation of Fig. 1b that would be consistent with previous studies directly testing the sea ice response to OHT[28,34,36]. On the other hand, sea ice loss removes a major insulator of the ocean, driving increased heat loss, which could ultimately be compensated by increased convergence of OHT. The magnitude of increased OHT would then be proportional to the amount of sea ice loss. Both hypothetical mechanisms are consistent with the data we have presented in Eq. (1), and are not mutually exclusive.

Lagged correlation analysis provides insight into (but does not prove) the relative degree of causation of the two mechanisms (OHT $\rightarrow \phi_i$ versus $\phi_i \rightarrow$ OHT), and our interpretation assumes that the two operate on different timescales. The mechanism in which increased OHT enhances sea ice loss, OHT $\rightarrow \phi_i$, relies on anomalous heat melting sea ice. In this case, we would expect to see a lag of zero to a few years in the sea ice response, depending on whether increased OHT directly melts ice or is released to and redistributed by the atmosphere (e.g., recent Barents Sea ice extent trends lag Atlantic OHT trends by about one year[39]). In the mechanism by which sea ice loss leads to increased heat release to the atmosphere, a compensating increase in OHT would require adjustment of the large-scale ocean circulation, such as the wind-driven gyres and overturning. Since these processes operate on multi-year timescales, in this case we would expect that $\Delta\phi_i$ leads ΔOHT by several years to decades. While this is a heuristic argument, it is supported by perturbation experiments in which simulated overturning circulations take more than 10 years to respond to abrupt, large-scale Arctic sea ice loss[84]. We

emphasise that this lagged analysis alone is not able to prove a causal relationship: this would require, for example, detailed examination of how changes occur in individual simulations, composite analyses, or causal-inference methods[85] beyond the scope of the present work. Combined with the EBM that shows where the relationship in Fig. 1b comes from, it merely provides a qualitative indication of the likely dominant direction of causality.

We find that $\Delta\phi_i$ and ΔOHT are maximally correlated with ΔOHT leading by around 5 years, which tends to support the OHT $\rightarrow \phi_i$ pathway (Supplementary Fig. 2a). However, there are still strong correlations within a ±20 year lag period so that we cannot rule out the $\phi_i \rightarrow$ OHT pathway. Asymmetry in the lagged correlation may indicate that the $\phi_i \rightarrow$ OHT pathway is not the primary mechanism but acts as a long-term feedback of the sea ice response to OHT. The correlation between ΔOHT and ΔT is not shown in Supplementary Fig. 2a but is almost identical to that between ΔOHT and $\Delta\phi_i$. This may reflect that most of the impact of OHT on Arctic sea ice occurs indirectly via the atmosphere and is captured by the ΔT term in Eq. (1). This is further supported by the lagged correlations with ΔAHT: ΔOHT leads ΔAHT (i.e., ΔOHT triggers Bjerknes compensation), while ΔAHT leads $\Delta\phi_i$ (Supplementary Fig. 2a), suggesting that OHT drives an atmospheric and ultimately sea ice response reminiscent of the so-called atmospheric bridge mechanism previously proposed[46]. However, this does not rule out the direct impact of OHT on sea ice (i.e., ocean heat release melts sea ice). Considering lagged correlations in models individually—those with at least 10 ensemble members (Table 1)—ΔOHT leads $\Delta\phi_i$ by a few years in four out of five cases (Supplementary Fig. 3a–e), suggesting the implied direction of causality is robust. However, ΔAHT only leads $\Delta\phi_i$ in two out of five cases, suggesting the underlying mechanism may not be consistent and/ or cannot be robustly detected by this method.

Southern Ocean

Here, we analyse simulations of Antarctic sea ice change over the historical and near-future periods in a similar way to the Arctic in the previous sections, considering the polar cap between 60°S and the south pole. Most simulations exhibit retreating Antarctic sea ice (ϕ_i, in degrees south, increases) over the historical period 1980–2021, and almost all exhibit net south-polar warming (Fig. 3a). The Antarctic sea ice edge sensitivity to surface temperature (1.1°S K^{-1}) is similar to that in the Arctic (1.4°N K^{-1}).
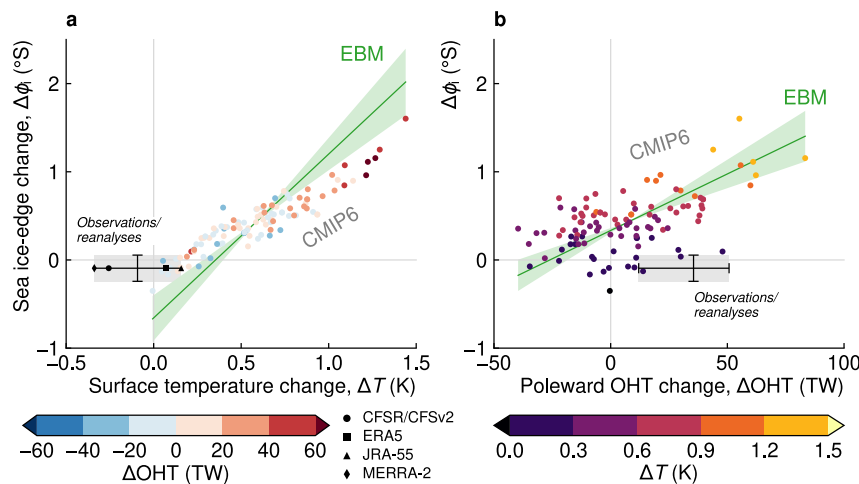

Fig. 3 | Antarctic sea ice, polar temperature, and ocean heat transport changes over 1980–2021. a Change in mean Antarctic sea ice-edge latitude, $\Delta\phi_i$, plotted against change in polar (latitudes poleward of 60°S) near-surface air temperature, ΔT, in CMIP6 simulations. Changes are computed as the difference in the 21 year means over 2000–2021 and over 1980–2000. Each point is an individual simulation, and its colour (blue–red scale) indicates the change in poleward ocean heat transport (ΔOHT; across 60°S, in units of 1 TW = 10^{12} W) between the same time periods. Estimates of the corresponding real-world changes are indicated by the vertical bar (uncertainty range derived from satellite observations of sea ice concentration) and

horizontal bar (different atmospheric reanalyses indicated by black symbols; see Methods). The energy-balance model (EBM) estimate of the sensitivity using Eq. (1) is shown by the green lines and shading (standard error propagated from underlying parameters), which is plotted through the ensemble mean. **b** As in (**a**) but with the OHT and temperature data switched, so that the former is plotted on the horizontal axis and the latter is shown by the colour (purple–yellow) scale. The horizontal bar represents an estimate of the real-world OHT change over this time period from the Estimating the Circulation and Climate of the Ocean (ECCO) ocean state estimate (see Methods).
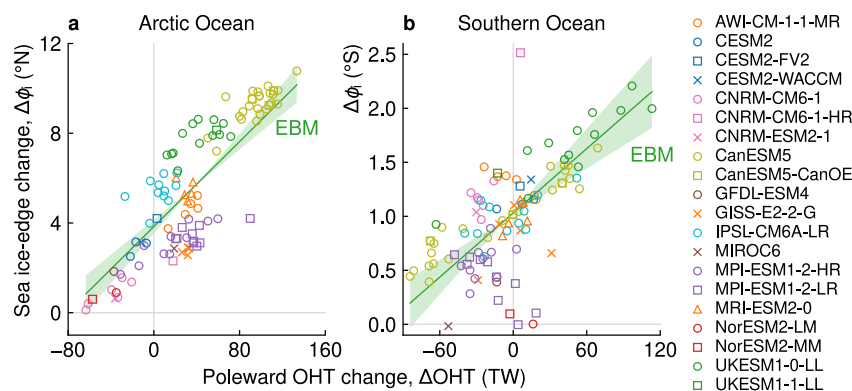
Fig. 4 | Near-future projected changes in sea ice and ocean heat transport. Change in mean sea ice-edge latitude, $\Delta\phi_i$, plotted against change in poleward ocean heat transport across (**a**) 65°N and (**b**) 60°S, ΔOHT, in CMIP6 historical and future (medium–high emissions scenario: SSP3-7.0) simulations for (**a**) northern and (**b**) southern hemispheres. Each point is an individual simulation (ensemble member) of the corresponding model listed in the legend. Changes are the difference in means of each quantity between periods 2030–2050 and 1980–2000. The energy-balance model (EBM) predicts the relationship between sea ice edge and OHT changes (green line, with standard error in shading) via the polar near-surface air temperature change and pre-industrial parameters that depend on large-scale radiative feedbacks (Eq. 1). The units of OHT are 1 TW = 10^{12} W.

Ninety-two percent of simulations warm faster than the fastest-warming reanalyses, and 87% exceed the upper estimate of Antarctic sea ice change, reflecting the substantial bias of the multi-model ensemble[17]. Figure 3b shows that, similarly to the Arctic, the relationship between the change in OHT across 60°S, ΔOHT, and $\Delta\phi_i$ is roughly linear but less correlated ($r = 0.55$) than that between ΔT and $\Delta\phi_i$ ($r = 0.93$). Antarctic sea ice exhibits around three times lower sensitivity to OHT than the Arctic, with a 1°S change associated with an OHT change on the order of 100 TW. About 40% of simulations exhibit decreases in OHT, but as in the Arctic the temperature and sea ice edge changes are almost all positive. The ECCO estimate suggests an increase in OHT into the Southern Ocean (horizontal bar in Fig. 3b) of a few tens of terawatts. Simulations with similar ΔOHT tend to have excessive Antarctic sea ice retreat and south-polar warming. While a few simulations exhibit realistic sea ice and OHT changes together (i.e., lying within the observational error bars in Fig. 3b), none are simultaneously consistent with real-world estimates of all three variables $\Delta\phi_i$, ΔT, and ΔOHT. Albeit with a large degree of scatter, unrealistic decreasing OHT at 60°S tends to result in smaller, more realistic Antarctic sea ice changes, contrasting with the Arctic in which realistic OHT is more closely associated with realistic Arctic sea ice retreat (cf. Figs. 1, 3).

Equation (1) is, by design and in principle, sufficiently idealised to also be applicable to the south polar cap. We thus determine 60°–90°S polar cap analogues of the various parameters to determine EBM estimates of Antarctic sea ice edge sensitivities to T and OHT (green lines in Fig. 3). The most substantially different parameter is S, which is almost 3 times larger in the southern compared to northern hemisphere (Fig. 5). This is a geometric effect relating to the different sensitivity of planetary albedo to a given poleward retreat of the ice edge—because the Antarctic sea ice edge spans most longitudes, whereas the Arctic ice edge is more restricted by land, a relatively small shift in the former is needed to expose the same amount of Southern Ocean and increase in net shortwave radiation as in the Arctic Ocean. Bjerknes compensation is present at 60°S, but interestingly the magnitude of AHT decreases just exceed associated OHT increases (i.e., an over-compensation; Fig. 6b), so that simulations exhibiting larger Antarctic sea ice loss do so with close to zero change or decrease in net meridional heat transport.

Equation (1) captures the multi-model behaviour although the fit between $\Delta\phi_i$ and ΔT is not as close as in the Arctic (Fig. 3b). However, the uncertainty (arising from non-perfect correlations between underlying variables in Eq. 1) and small signal-to-noise ratio (compared to the Arctic) should be taken into account. The EBM is also better aligned with CMIP6 when using the more tightly-constrained sea ice–temperature relationship (Fig. 3a) to estimate the emergent sensitivity of Antarctic sea ice to OHT (Fig. 3b). We explore other possible reasons for the bias in Fig. 3a in the 'Discussion' section.

We also repeat the lagged correlation analysis for an indication of the likely direction of causality in the Southern Ocean. We find that ΔOHT is maximally correlated with $\Delta\phi_i$ when the latter leads by around 8 years (although again there are still significant correlations at zero lag; Supplementary Fig. 2b). This suggests that OHT change in the Southern Ocean is mainly a response to, not a driver of, changes in Antarctic sea ice in CMIP6 models. Here, OHT change is more strongly correlated with AHT at substantial lags so that AHT leads both the OHT (i.e., Bjerknes compensation initiated by the atmosphere) and sea ice changes. Changes in OHT lagging sea ice loss is robust to repeating the analysis on individual models, except for one out of five cases (the same model, MPI-ESM1-2-LR, that is also inconsistent in the Arctic; Supplementary Fig. 3f–j). However, the patterns of lagged correlation vary among individual models, suggesting less inter-model consistency compared to the Arctic.

Future projections

We extend our analysis to future projections by considering the time difference of OHT, T, and ϕ_i between the average over the near-future period 2030–2050 and that over 1980–2000. Restricting to the mid-twenty-first century limits the number of simulations that are seasonally or completely ice free. Figure 4a highlights the magnitude of inter-model spread in the Arctic. Remarkably, some models show almost no change in Arctic sea ice over this time period while, under the same imposed CO_2 emissions, some exhibit more than 10°N of sea ice retreat. The two cases correspond to a reduction and substantial increase in OHT, respectively. Inter-model spread in near-future sea ice change, $\Delta\phi_i$, is related to the spread of ΔOHT via the future polar air temperature change, ΔT, and the atmospheric processes of Bjerknes compensation and radiative feedbacks contained in the coefficients of Eq. (1). Models are largely separated in Fig. 4a, without much overlap of ensemble members from neighbouring models. Examining individual members, internal relationships between ΔOHT and $\Delta\phi_i$ are not always apparent (e.g., orange triangles for MRI-ESM2-0). Structural model biases outweigh internal variability in the spread of Arctic sea ice projections[86,87], seen here with the added context of OHT.

The Southern Ocean also exhibits a multi-model relationship between $\Delta\phi_i$ and ΔOHT (Fig. 4b). Unlike the Arctic, there is more overlap of ensemble members from different models, indicating a greater role of natural variability. There are several conspicuous outliers, however, that suggest a breakdown of the relationship. The high-resolution CNRM-CM6-1-HR shows the largest Antarctic sea ice loss and has an OHT change of order 100 TW smaller than expected based on the EBM. It has the largest AHT decrease, departing from the multi-model Bjerknes compensation relationship (Fig. 7b) but consistent with our previous deduction that Antarctic

sea ice changes are primarily atmosphere-driven. This example demonstrates the potentially large impact of model resolution, since its low-resolution counterparts (pink circles and crosses in Fig. 4b) are more in line with the other models. Taken alone, MPI-ESM1-2-LR (purple squares) exhibits negative correlation between ΔOHT and $\Delta\phi_i$, unlike the high-resolution version (purple circles), again suggesting a large impact of resolution on the qualitative behaviour under climate change.

Discussion

The Arctic will likely become seasonally sea ice-free in the coming decades[88–93], impacting the local and remote environment[94–97]. Constraining the timing as a function of global warming level is of societal concern and calls for reliable projections. Our analysis indicates an offsetting or enhancing effect of OHT on Arctic sea ice loss until at least 2050, which is about when CanESM5, the model in our sample with the largest OHT increase (Fig. 4a), becomes seasonally ice free[98]. In contrast, CNRM-CM6-1, the model exhibiting the strongest decrease in OHT, becomes seasonally ice free around 2080[98], beyond the time span we have analysed. Assuming OHT continues to affect sea ice loss in this way at least until the summer ice disappears, these examples suggest about 140 TW of OHT (Fig. 4a) is associated with a 30 year earlier emergence of seasonally ice-free conditions. The timing also depends on how much sea ice there is to lose in the first place. Since there is also correlation between the mean states of sea ice and OHT[44–46], the dependence of the ice-free Arctic on OHT is non-trivial and warrants further study.

Most of the spread of the change in Arctic sea ice over the historical and future periods is due to model differences rather than natural variability (Fig. 4a). Our work thus implies that, for future Arctic sea ice projections, reduced uncertainty is within reach through a better understanding of, and ultimately addressing, causes of ocean biases. Illustratively, recent work suggests that specific ocean models may have a systematic impact on the simulation of the Arctic[47]. Investigation of ocean biases entails validation of models against the real world. An observational estimate of the 1980–2021 OHT change is included in our analysis, but it is only a rough estimate based on partial data coverage due to sparse sampling of the ocean (e.g., with the Argo period started in the early 2000s). This highlights the need for continuous monitoring of transports through the major Arctic gateways and extension of ocean analyses, in order to identify whether models simulate realistic Arctic sea ice trends for the right physical reasons.

While the EBM captures the Arctic behaviour well, its success in explaining the Southern Ocean is less convincing (Fig. 3a). It might be suggested that averaging over 60°–90°S is too broad of a domain to average surface temperature and vertical radiative heat fluxes because a large fraction (35%) of it is occupied by the Antarctic continent. The Antarctic ice sheet has a substantial impact on the south polar, large-scale radiative heat balance[99], so that by applying the EBM to the whole polar cap we are implicitly including Antarctic processes not relevant to the sea ice. In contrast, while there is considerable land cover in the Arctic, it is mostly distributed around the periphery of the northern domain (Fig. 2): the ice-edge latitude diagnostic accounts for this (see Methods) and Arctic sea ice extends to the north pole. Equation (1) is easily modified to consider the domain between two latitudes (see Methods). We could eliminate the Antarctic continent using the zonal-average latitude of its coastline, 72°S (median), as the second reference latitude (i.e., consider 60°–72°S) keeping with the zonal-average spirit of the EBM (Supplementary Fig. 4). However, this has little impact on the bias of the EBM fit to $\Delta\phi_i/\Delta T$ (Supplementary Fig. 5a), suggesting that Antarctic radiative processes are not responsible for the discrepancy between the EBM and CMIP6-emergent sensitivity of sea ice to surface temperature. Another factor could be increased cloud cover in response to sea ice loss offsetting top-of-atmosphere albedo changes, and hence the large-scale energy balance[100]. Yet we also find negligible impact when using a climate-change-derived (as opposed to pre-industrial derived) value of S in Eq. (1). We argue that the more likely explanation for the bias in Fig. 3a is simply that the inter-model relationship between sea ice and OHT is weaker in the Southern Ocean. Removing models that are identified as outliers (i.e., inconsistent with the majority) in the future projections (Fig. 4b) moves the EBM sensitivity closer

to CMIP6 in the historical period (Supplementary Fig. 6). Perhaps surprisingly, one such removed model, MPI-ESM1-2-LR, is one of the closest to concurrently simulating realistic changes in sea ice, surface temperature, and OHT over the historical period (Supplementary Fig. 6), yet does not exhibit significant correlations between OHT and sea ice or temperature, and has the opposite sign of Bjerknes compensation (Supplementary Fig. 3i).

There is an inherent approximation in treating transient simulations with a steady-state framework. Specifically, the EBM considers two averaging periods as distinct, equilibrium climate states, where the change in variables between the two (ΔOHT, etc.) comprises the associated climate adjustment. In other words, there is an assumption of quasi-equilibrium, but in practice, there are longer-timescale internal processes mixed with the time-varying external forcing invalidating this assumption. These are likely relevant in the Southern Ocean judging from the lagged-correlation analysis (Supplementary Fig. 2b). That analysis also suggests that Southern OHT and Antarctic sea ice changes are led by atmospheric circulation changes, despite the negative relationship between ΔAHT and $\Delta\phi_i$ associated with Bjerknes compensation. Thus, unlike the Arctic, the intuitive correlation between ΔOHT and $\Delta\phi_i$ in the Southern Ocean may be a red herring in the context of inter-model spread in Antarctic sea ice. Overall, further work is required to better understand the nature of the OHT–sea ice relationship in the southern hemisphere. Analysing the internal variability of a single model would enable us to verify whether the EBM is lacking a physical process or represents one overly simplistically in the Southern Ocean. Conversely, it is worth investigating why models do not behave consistently in the Southern Ocean while they do appear to in the Arctic: which processes lead to qualitatively divergent behaviours (i.e., the scatter in Fig. 3b)?

Our results attest to the ongoing utility of the classical EBM literature for shedding new light on problems in contemporary climate science. There are many ways that heat may be redistributed between the atmosphere, ocean, and sea ice, and in or out of the polar region, but there is a fundamental constraint of energy conservation. This constraint is the foundation of the EBM. Yet, the derived Eq. (1) goes beyond mere energy conservation by combining the correlated and linear processes of radiative feedbacks (R), albedo impact of sea ice (S), Bjerknes compensation, and ocean heat budget (C). Accounting for this physics in a simple manner yields a quantifiable, three-way relationship between OHT, sea ice, and temperature, that climate models closely follow as an emergent phenomenon. For the Arctic, the EBM thus provides a physical grounding to inter-model spread of sea ice and OHT change that was missed by previous studies focusing on correlations. It explains not only the sign but also the size of inter-model spread in sea ice projections as a function of simulated OHT change (leading to the sensitivity of about 3°N per 100 TW OHT into the Arctic; Fig. 1b). It also tells us the other relevant processes to consider in our lagged-correlation analysis which implies that, in the Arctic, OHT mainly leads changes in the atmospheric variables and sea ice. Although more work is needed to robustly quantify the mechanisms and degree of causality, this is consistent with recent efforts to elucidate causal drivers of Arctic sea ice loss in a different approach of measuring information flow[85], strongly pointing to OHT as a major driver of model spread.

Methods

Energy balance model

Equation (1) is developed from an existing EBM framework[62] which is a two-layer (atmosphere and ocean mixed layer/sea ice), zonal-average, thermodynamic toy model of the climate of one hemisphere. There is no explicit account of land so the system may be applied symmetrically to both hemispheres. For present purposes, we do not require details of the parameterisations for sea ice thermodynamics, shortwave radiation and albedo, OHT, or AHT, and need only consider the region between the reference latitude ϕ_0 and the pole. This polar cap, reduced version of the EBM is depicted in Fig. 2 for the Arctic.

Changes in the rate of heat entering or leaving the domain via the top of the atmosphere (TOA) and at ϕ_0 must match any change in the rate of heat storage. At the TOA, such changes occur via the outgoing longwave radiation, F_{OLR}, and net shortwave radiation, F_{sw}, while at the boundary ϕ_0,

changes occur via AHT and OHT:

$$A\Delta F_{sw} - A\Delta F_{OLR} + \Delta AHT + \Delta OHT = \Delta \partial_t H, \qquad (2)$$

where $A = 2\pi a^2 (1 - \sin\phi_0)$ is the total surface area of Earth, radius a, between latitudes ϕ_0 and the pole. The vertical heat fluxes ΔF_{sw}, ΔF_{OLR}, and others defined in the following (Eqs. 6–8), are averages over the polar cap so that, e.g., AF_{sw} is the net shortwave radiation integrated over the domain. It is assumed that the system stores all heat in the ocean, letting $\partial_t H$ be the rate of ocean heat uptake (integrated over the ocean part of the polar cap). Rearranging Eq. (2):

$$\Delta F_{sw} = \Delta F_{OLR} - \frac{1}{A}\left(1 + b_c - h\right)\Delta OHT, \qquad (3)$$

where, as described in the main text, ΔAHT is expressed in terms of the rate of Bjerknes compensation:

$$b_c = \frac{\Delta AHT}{\Delta OHT}. \qquad (4)$$

We have also defined and used:

$$h = \frac{\Delta \partial_t H}{\Delta OHT}, \qquad (5)$$

which may be interpreted as an efficiency of OHT anomalies in modifying the rate of ocean heat uptake.

In the two-layer EBM, OLR depends on the temperature of the atmosphere[57,62], which is coupled to the surface via upwelling longwave radiation and turbulent fluxes defined in the upward component, F_{up}, and downwelling longwave radiation, F_{down} (Fig. 2). These fluxes are expressed as linear functions of the surface, T, and air, T_a, temperatures:

$$\Delta F_{up} = B_{up}\Delta T \qquad (6)$$

$$\Delta F_{down} = B_{down}\Delta T_a \qquad (7)$$

$$\Delta F_{OLR} = B_{OLR}\Delta T_a, \qquad (8)$$

where T_a refers to some mid-troposphere height such as 700 hPa[62,98] or 500 hPa[57,61]. Linear approximations such as these have been widely utilised in EBM studies[57,59–62], and the suitability of the particular versions in Eqs. (6–8) have been demonstrated using reanalysis data[62,98]. Each B in Eqs. (6–8) is a constant, bulk parameterisation representing primarily radiative feedbacks and are remarkably consistent across models[98]. For the present work, we do not require T_a, so eliminate it by considering the energy balance of the atmospheric layer alone:

$$A\Delta F_{OLR} + A\Delta F_{down} = A\Delta F_{up} + \Delta AHT, \qquad (9)$$

where the absence of shortwave radiation is due to a common assumption in EBM literature, also adopted here, that atmospheric absorption of shortwave radiation is negligible. Using Eqs. (6–8), rearranging for ΔT_a, then multiplying by B_{OLR} gives an expression for ΔF_{OLR} in terms of surface rather than air temperature:

$$\Delta F_{OLR} = \frac{\beta B_{up}}{1+\beta}\Delta T + \frac{\beta b_c}{A(1+\beta)}\Delta OHT, \qquad (10)$$

where we have again utilised the Bjerknes compensation rate and defined:

$$\beta = \frac{B_{OLR}}{B_{down}}. \qquad (11)$$

For ΔF_{sw}, the net absorbed shortwave radiation, we assume (and show in Fig. 5e–f) that this scales approximately linearly with the sea ice-edge latitude, so that:

$$\Delta F_{sw} = S\Delta\phi_i. \qquad (12)$$

The parameter S incorporates effects such as the planetary albedo difference between sea ice and open ocean, changes in cloud distribution, and geometric factors[61,62,98]. Substituting this and Eq. (10) into Eq. (3), and collecting terms, gives:

$$S\Delta\phi_i = \frac{\beta B_{up}}{1+\beta}\Delta T - \frac{1}{A}\left(1 + \frac{b_c}{1+\beta} - h\right)\Delta OHT. \qquad (13)$$

The main text Eq. (1) follows from Eq. (13) by defining R and C as the coefficients of the terms on the right-hand side:

$$R = \frac{\beta B_{up}}{1+\beta}, \qquad (14)$$

and:

$$C = \frac{1}{A}\left(1 + \frac{b_c}{1+\beta} - h\right). \qquad (15)$$

Manifest in Eq. (13) is the previous finding that sea ice is intrinsically less sensitive to AHT than OHT, i.e., the sea ice response to a change in AHT when OHT is fixed is less than that of the equivalent OHT change when AHT is fixed[59,62]. This means that even in the limit of perfect Bjerknes compensation, i.e., $b_c = -1$, the impact of OHT is not cancelled out by compensation of AHT. This effect is expressed by the factor of $(1+\beta)^{-1}$ that quantifies the proportion of AHT convergence lost to space via OLR rather than radiated to the surface to melt ice[59,62]. Additionally, anomalous OHT only affects the surface climate at all if the heat is released via surface fluxes rather than adding to the heat storage (see Eq. 16, below). The h term quantifies the latter (Eq. 5), which offsets the impact of OHT on surface variables ϕ_i and T. The coefficient of ΔOHT, i.e., C, can thus be thought of as a correction factor accounting for these processes.

In the main text, we discussed using a reduced domain for the southern hemisphere analysis by restricting to a latitude band ϕ_0–ϕ_1 for $\phi_1 < 90°$S. This requires a modification to the EBM equation: in the derivation, Eq. (2) has additional OHT and AHT terms on the right-hand side each being evaluated at the second, poleward reference latitude ϕ_1 (see Supplementary Fig. 4). These additional terms can be simply combined into a difference of integrated OHT and AHT convergences, OHTC = OHT(ϕ_0) − OHT(ϕ_1), and similarly for AHTC. The other vertical heat fluxes (heat content tendency change) are re-interpreted as averages (integrals) over the latitude band ϕ_0–ϕ_1. The rest of the derivation follows as in Eqs. (2–13), again replacing ΔOHT with $\Delta OHTC$. In Supplementary Fig. 5, we absorbed the factor of A in the second term on the right-hand side of Eq. (13) into $\Delta OHTC$ to make the units more intuitive for heat convergence (i.e., W m^{-2}), but note that this is only the approximate OHTC since A is the area of the whole latitude band, not just the ocean part of that domain.

Model selection

Table 1 lists the models and ensemble members included in our analysis, and their references for details of components, resolutions, configurations, and performances. We include all models providing the output fields required, for both the historical[101] and SSP3-7.0[102] experiments. The analysis of the historical period (i.e., Figs. 1 and 3) is extended to include years 2015–2021 from the SSP3-7.0 experiment, which is also used for the future analysis (i.e., Fig. 4). This scenario is chosen because of maximum data availability, i.e., giving us the largest total number of ensemble members.

Fig. 5 | Atmospheric radiation parameters derived from CMIP6 pre-industrial control simulations. a Anomalies (relative to model means) of surface upwelling longwave radiation and net upward turbulent heat flux, ΔF_{up}, plotted against near-surface temperature, ΔT, each being averaged over 65°–90°N. The points are 21-year averages from the pre-industrial control simulations of the CMIP6 models listed in Table 1. The slope of this data gives our estimate of B_{up} for the northern hemisphere, determined by orthogonal distance regression shown by the red line. The stated uncertainty is the standard error of this regression. The legend also gives the correlation coefficient, r. **b** As in (**a**) but for the southern hemisphere, with averages over 60°–90°S. **c** Top-of-atmosphere outgoing longwave radiation, ΔF_{OLR}, plotted against downwelling longwave radiation at the surface, ΔF_{down}, temporally and spatially averaged in the same way as ΔF_{up} and ΔT in (**a**). Here, the slope gives β for the northern hemisphere. **d** As in **c** but for the southern hemisphere. **e** Surface net shortwave radiation, ΔF_{sw}, plotted against sea ice-edge latitude, $\Delta \phi_i$, temporally and (for the former) spatially averaged in the same way as ΔF_{up} and ΔT in (**a**). Here, the slope gives S for the northern hemisphere. **f** As in (**e**) but for the southern hemisphere.
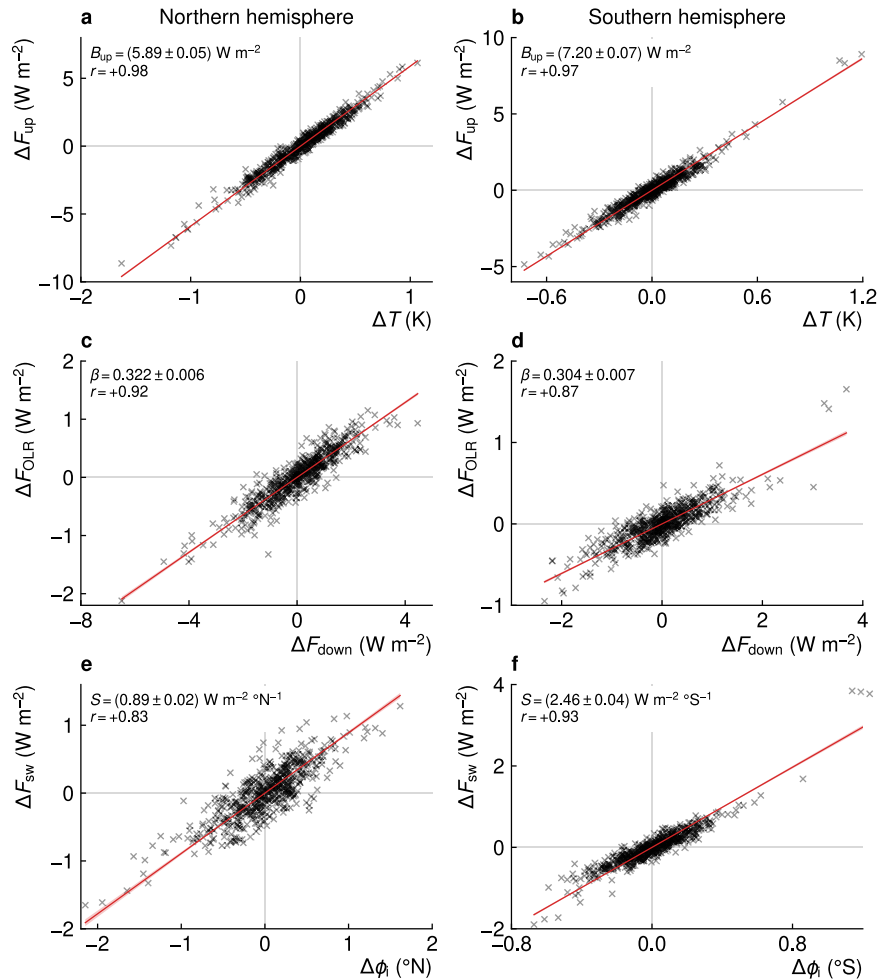
Still, we note that using a different future scenario does not alter the EBM results[98]. All models except two provide the necessary data from a pre-industrial (PI) control simulation, of varying lengths (Table 1), that we use to compute some of the parameter values in Eq. (13).

Sea ice-edge latitude

This is computed from monthly-mean sea ice concentration fields, which are first linearly interpolated onto a regular, independent longitude/latitude grid of similar resolution to the nominal ocean grid of each model (Table 1). An exception is GISS-E2-2-G, for which sea ice concentration is already on a regular grid and so does not require interpolation. Then, for each hemisphere, we apply an algorithm that identifies the ice edge (15% concentration) latitude at each longitude, excluding such points that are too close to land as these obscure the seasonal cycle of ice cover in the final, zonal average metric[103]. We use the default options (100 km minimum distance from land and selecting the most equatorward ice edge in ambiguous cases) of the existing code implementing this algorithm[46,104]. We then take the zonal-mean ice edge latitude as ϕ_i in each hemisphere. This calculation is done for each month before taking annual averages and then averaging over the 21 year periods as described in the main text. We note that ϕ_i calculated in this way is directly proportional to sea ice extent and area when considering averages over such multi-decadal timescales[46]. However, ϕ_i gives an arguably more intuitive measure of sea ice change (i.e., in terms of degrees of latitude), correctly factors out the impact of land/geometric constraints that are irrelevant to the thermodynamics, and it naturally arises in the zonal-mean EBM framework.

Surface temperature

The near-surface air temperature is readily available on the atmospheric grid at monthly-mean frequency. The GMST (Supplementary Fig. 1) is its area-weighted average over the globe, then averaged annually and over 21 year periods as required. For the Arctic polar-average temperature, T, the calculation is restricted to latitudes poleward of the reference latitude 65°N, and for the Southern Ocean poleward of 60°S (main text, Figs. 3 and 4b), or between 60°–72°S for the reduced-domain analysis presented in Supplementary Fig. 5; see 'Reference latitude' section.

Ocean heat transport and storage

Several ocean model outputs are relevant here. First, 'hfbasin' is the depth-integrated, net northward ocean heat transport integrated within basins, obtained by integration of the heat flux along a zigzag path of native ocean grid cell boundaries approximating a line of constant latitude[105]. However, not all models provide this and, for some which do, data inspection reveals that the zonal integration has been carried out along grid rows, for which latitude varies on curvilinear grids (especially in the polar regions), rather than the zigzag paths specified by OMIP protocols[105]. We also require ocean heat storage tendency, $\partial_t H$, for application of Eq. (13), which is obtained by summing vertically the output 'opottemptend', the ocean potential temperature tendency expressed as heat content (alternatively, 'ocontemptend', the conservative temperature tendency expressed as heat content, where applicable). This quantity, in combination with the net downward surface flux, F_{surf} (model output 'hfds', widely available), can also yield OHT as a residual if 'hfbasin' is unavailable or unusable. This follows from the ocean heat budget (direct model outputs underneath each term):

$$\underbrace{\partial_t H}_{\text{opottemptend}} = \underbrace{F_{surf}}_{\text{hfds}} - \nabla \cdot \underbrace{OHT}_{\text{hfbasin}}. \qquad (16)$$

Unfortunately, few models provide the heat content data directly. In these cases, if the 'hfbasin' data is available and usable then, together with 'hfds', $\partial_t H$ can be computed as a residual (also using Eq. 16). If both 'hfbasin' and 'opottemptend' are unavailable or unusable, another option is to use the depth-integrated horizontal heat transport components 'hfx' and 'hfy', aligned along the native ocean grid directions, to calculate OHT directly. Then, $\partial_t H$ can be computed as a residual using 'hfds' and Eq. (16). As such, there are three methods to calculate OHT and $\partial_t H$, depending on data availability for each model, summarised and expanded upon as follows:

1. **Residual**: OHT convergence is calculated as a function of position on the native grid by subtracting the net downward surface flux, F_{surf} (model output 'hfds'), from the heat storage tendency, $\partial_t H$ (model output 'opottemptend'), following from Eq. (16). The OHT convergence is then integrated (area-weighted sum) over all grid cells with latitude $\phi > \phi_0$ to approximate the OHT across ϕ_0. The raw data 'opottemptend' are obtained as yearly means, while 'hfds' is retrieved monthly but averaged annually for the calculation.

2. **hfbasin**: if this output is available, we check its computation has been carried out along zigzag paths and if so use it directly for OHT, linearly interpolating to reference latitudes ϕ_0. If 'opottemptend' is not available to give $\partial_t H$ directly, then the 'hfbasin' data is used to calculate it as a residual using the 'hfds' data and Eq. (16). The 'hfbasin' raw data are monthly means.

3. **hfx/hfy**: the two heat flux components are assumed to be situated at top and right grid-cell (ocean column) edges, as in an Arakawa C-grid configuration that the four models requiring this method use (Table 1)[106–108]. First we compute the net horizontal heat flux entering each grid cell (subtracting the top and right edge fluxes from the sum of the bottom and left edge fluxes, the latter being associated with neighbouring cells). Dividing by the grid cell areas then gives the OHT convergence, which follows from the divergence theorem. Then integrating everywhere poleward of ϕ_0 gives the OHT across ϕ_0. Finally, $\partial_t H$ is calculated as a residual using Eq. (16). The raw data 'hfx' and 'hfy' are retrieved as monthly means. Table 1 lists the method used for each model, illustrating an inconsistency of ocean heat transport and heat storage data availability in CMIP6—despite the 'hfbasin' diagnostic being priority 1[105,109]. A fourth method could be to compute OHT from the currents and temperature fields on the native grid, but this would require a very large data volume. It is also a non-trivial calculation in terms of closing heat budgets, choice of reference temperature, accounting for the transport by sub-gridscale eddies, and different ocean grid geometries. It is worth stating that our model sample size is substantially limited by ocean data in general. We estimate that there are about 70 coupled atmosphere–ocean model variants in the CMIP6 archive contributing data for the historical and ScenarioMIP experiments that we could potentially have included. Only 29 of those provide some combination of ocean diagnostics suitable for computing OHT and $\partial_t H$. We are not the first to highlight difficulties in obtaining OHT estimates for multi-model analyses[82] and we wish to echo and emphasise the importance of wider availability and accurate diagnostics of ocean transports and storage.

Atmospheric heat transport

Atmospheric heat transport (AHT; more precisely the moist static energy transport) at latitude ϕ_0 is diagnosed by integrating the net heat flux into the atmospheric column over all latitudes poleward of ϕ_0. Since the atmosphere data are on regular longitude/latitude grids, we first integrate poleward of grid cell boundaries to get the exact transport at those latitudes, then interpolate to the required reference latitudes. This minimises errors and any biases resulting from differences in model resolutions. The net heat flux is calculated from TOA radiation (net shortwave and OLR), surface upwelling and downwelling shortwave and longwave radiation, and surface sensible and latent heat fluxes. These fields are obtained as monthly means for the calculation of AHT, then averaged annually and over the required multi-decadal time periods. This method has been used in previous studies[80,82].

Reference latitude

In the Arctic we use $\phi_0 = 65°N$. This is south of the zonal-mean winter Arctic sea ice edge for most models during the PI era[46]. We find negligible sensitivity to the results (correlation between ΔOHT and ΔT and the extent to which it is captured by the EBM) to ϕ_0 in the Arctic for $\phi_0 = 55°–65°N$. For the Southern Ocean, we choose $\phi_0 = 60°S$ as this intersects Drake Passage (i.e., includes all longitudes of ocean) and is sufficiently far from Antarctica to enclose the sea ice edge of most models and observations. In the supplementary reduced-domain analysis, in which we consider a restricted latitude band (Supplementary Figs. 4, 5), the poleward boundary latitude is chosen to be 72°S. This is the zonal-median latitude of the Antarctic coast, which we determined using coarse-scale coastline data from Natural Earth (https://www.naturalearthdata.com/).

Parameter values for the EBM

Each parameter in Eq. (13) is a ratio of two quantities, so we require the slope of a linear fit that we estimate using orthogonal distance regression (ODR). This minimises the sum of perpendicular distances between data points and the fitted line. It does not require either variable to be independent and avoids biases of regression dilution that would otherwise occur using traditional, ordinary least-squares regression[110]. Specifically, if the ODR slope of y on x is $m \pm \delta m$, then the ODR slope of x on y is $1/m \pm \delta m/m^2$ (taking the reciprocal of one gives the other). In other words, the result does not depend on which variable of a given pair is regressed onto the other. This method is also used to estimate the sensitivities from the data without the EBM (e.g., the slopes of data in Figs. 1, 3, and 4, as quoted in the main text).
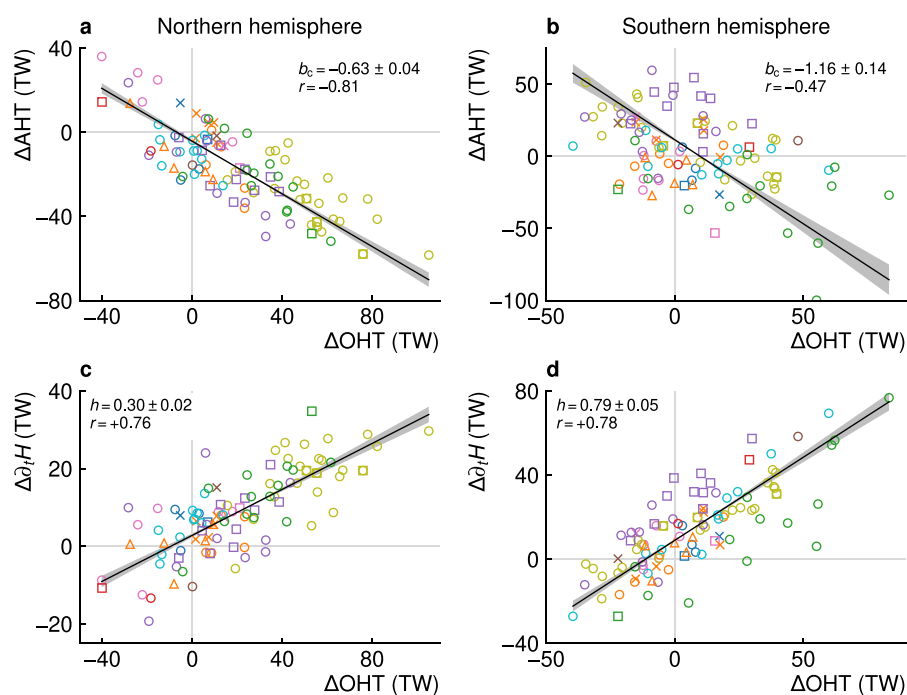
The PI control simulations of the 18 models that provide the required data (Table 1) are used to calculate values of S (Eq. 12), as well as B_{up} and β giving R (Eq. 14), for use of the EBM Eq. (13). Relevant data in each case, detailed below, are retrieved as monthly means. Contiguous 21-year averages are taken, discarding remainder years at the end of the time series (most PI-control simulation lengths are not multiples of 21 years; see Table 1). For each model and for each quantity Q, the mean over the whole simulation (less any remainder years) is subtracted to obtain 21-year anomalies ΔQ. Parameters are calculated separately for each hemisphere.

Values of B_{up} are estimated by plotting the net upward heat flux at the surface (upwelling longwave radiation and net upward sensible and latent heat) against the near-surface temperature (see Eq. 6). These fields are prepared according to the description above and area-weighted spatial averages are computed over the region between the reference latitude ϕ_0 and the pole. Figure 5a shows this data for the northern hemisphere and illustrates the validity of Eq. (6). The diagnostics ΔF_{up} and ΔT are highly correlated ($r = 0.98$) and there is a strong linear relationship. The slope of all points gives an estimate of B_{up}, and we use the standard error of regression as its uncertainty. This is repeated for the southern hemisphere (Fig. 5b).

This procedure could be used to determine B_{down} and B_{OLR}, replacing the heat fluxes and temperature according to Eqs. (7) and (8) respectively. However, since the EBM Eq. (13) only depends on $\beta = B_{OLR}/B_{down}$, it is simpler to directly estimate the ratio of the two parameters. This avoids the choice of reference pressure level for air temperature T_a (relevant to EBMs in general but not the present study) and the compounding of regression errors of two terms rather than one. We obtain, prepare as described above, and plot, the OLR against surface downwelling longwave radiation. The two radiative fluxes are again highly correlated ($r = 0.9$) and linearly related. The regression estimates of β are similar in each hemisphere (Fig. 5c, d).

The sea ice/shortwave radiation parameter, S, is computed from anomalies in sea ice-edge latitude, $\Delta \phi_i$, and net surface solar radiation, ΔF_{sw} (Eq. 12). Surface reflected (upwelling) shortwave radiation is subtracted from the incident (downwelling) shortwave radiation and averaged between the reference latitude ϕ_0 and the pole. There is little difference to S when TOA shortwave fluxes are used instead, validating the assumption used in Eq. (9) that atmospheric absorption of shortwave radiation can be neglected. The slope of the data in Fig. 5e–f gives S for each hemisphere. The high correlations ($r \sim 0.9$) justify the application of Eq. (12).

Fig. 6 | Ocean parameters derived for the energy-balance model equation for the historical period.
a Change in poleward atmospheric heat transport, ΔAHT, plotted against that of ocean heat transport, ΔOHT, evaluated at 65°N. Each point is a difference in means over the two 21-year periods 1980–2000 and 2001–2021, for each simulation of the CMIP6 models listed in Table 1 (see also the legend of Fig. 4). The slope of this data gives the Bjerknes compensation rate, b_c, used in the energy-balance model (EBM) equation, determined by orthogonal distance regression, shown by the black line and grey shading. The legend states the slope value and its standard error, as well as the correlation, r, of the data. **b** As in (a) but for the southern hemisphere (heat transports evaluated at 60°S). **c** Change in rate of ocean heat uptake, $\Delta\partial_t H$, over the same time periods, plotted against ΔOHT. The slope of this data, determined similarly, gives the parameter h defined in Eq. (5). **d** As in (c) but for the southern hemisphere.

The OHT correction factor C of the EBM Eq. (13) requires the Bjerknes compensation rate, b_c (Eq. 4), and the OHT efficiency parameter, h (Eq. 5). These are strongly dependent on the background climate. Specifically, Bjerknes compensation does occur in the unforced variability of the PI control simulations[46,82], but there the TOA fluxes are relatively constant compared to the climate change scenarios we examine here, so that the rate of compensation, b_c, is different. In the PI control, ocean heat content tendency, $\partial_t H$, is essentially a noise term that has little relationship with OHT anomalies (e.g., $r \sim 0.3$ in the Arctic). Therefore, h is poorly defined for the PI era (and would be set to zero in Eq. 13). Here, b_c and h must instead be determined from the forced changes in AHT, OHT, and $\partial_t H$ during the historical and future periods as required.

Figure 6a plots, for the northern hemisphere, the change in AHT in each model simulation against the OHT change, where changes are the difference in 21 year means over the periods 1980–2000 and 2001–2021. In other words, the OHT data are the same as that plotted in Fig. 1a. The slope of this data gives the northern hemisphere b_c for the historical period. Similarly, Fig. 6c plots the change in area-integrated ocean heat uptake tendency, $\Delta\partial_t H$, against ΔOHT. This gives the parameter h (Eq. 5) that along with b_c (and β determined from the PI data) is used in Eq. (15) and then (13) to determine the EBM sensitivities in Fig. 1. The same procedure generates the southern hemisphere parameter values (Fig. 6b, d), and we do this separately for the near-future period (2030–2050; values shown in Fig. 7 are used to determine the EBM sensitivities in Fig. 4).

The EBM parameters are computed from and combined with the CMIP6 data and fed into Eq. (13) after rearranging for $\Delta\phi_i/\Delta T$ (Figs. 1a and 3a) or $\Delta\phi_i/\Delta$OHT (Figs. 1b, 3b, and 4). This gives the slopes of the EBM lines on Figs. 1, 3, and 4, which are plotted through the ensemble-mean data point (the EBM says nothing of the intercept of this data). Errors on each parameter or other term in the equation are taken as the standard error of ODR regression and are propagated to the final result, represented by the green shading on these plots.

Observational estimates
Passive-microwave observations of sea ice concentration are obtained from the National Snow and Ice Data Center (NSIDC) at monthly-mean frequency for the 42 year period 1980–2021. Two datasets exist based on different metho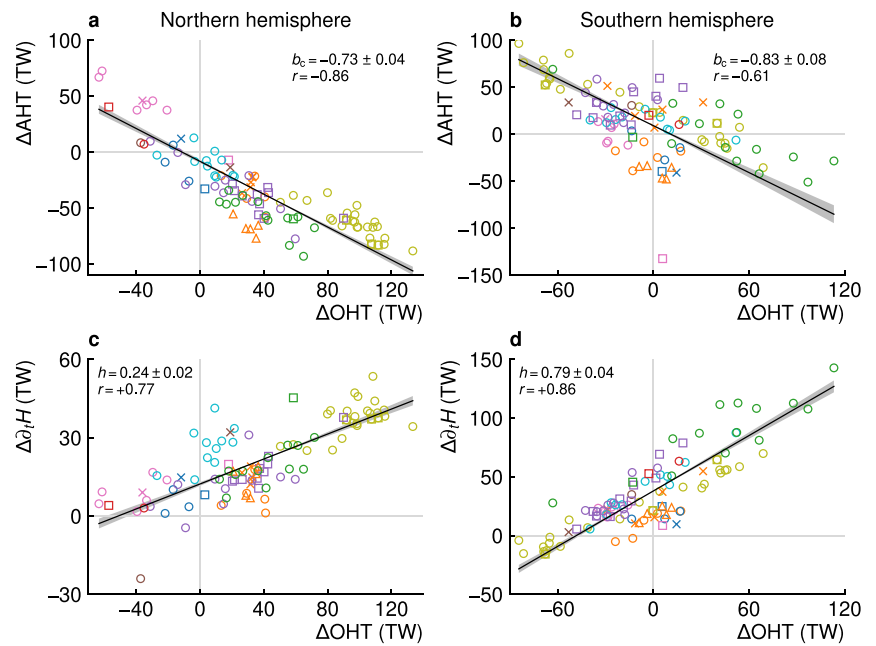ds to convert brightness temperature to sea ice concentration: the NASA Team and Bootstrap algorithms[111]. We calculate time series of the zonal mean sea ice-edge latitude in the same way as for CMIP6 model data (see 'Sea ice-edge latitude' section), for both sea ice concentration algorithms, for each hemisphere. The average ice edge latitude is calculated for the first (1980–2000) and second (2001–2021) 21-year periods. The vertical bars on Figs. 1 and 3 and Supplementary Figs. 1, 5, and 6 are determined by the minimum and maximum changes from the first to the second time average that can possibly be calculated by combining both algorithms. For the Southern Ocean, despite the 2016 unprecedented sharp decline in Antarctic sea ice extent that did not fully recover in subsequent years[16], our quantification using 21-year means yields, on average, a slight decrease in ϕ_i. However, the uncertainty range includes zero, consistent with the latest IPCC report that there has been no significant overall trend over 1979–2020[24].

Figures 1a and 3a and Supplementary Figs. 1, 5, and 6 require estimates of the real-world polar-averaged or global-average surface temperature changes. Reanalyses are used rather than pure, direct observations because the latter are too sparse in the polar regions. We include estimates from the following four state-of-the-art atmospheric reanalyses, and take the range of values as an estimate of the uncertainty:

- National Centers for Environmental Prediction (NCEP) climate forecast system reanalysis (CFSR/CFSv2)[112,113]
- European Centre for Medium-Range Weather Forecasts (ECMWF) Reanalysis version 5 (ERA5)[114]
- Japan Meteorological Agency (JMA) second Japanese global atmospheric reanalysis (JRA-55)[115]
- NASA Global Modeling and Assimilation Office (GMAO) Modern-Era Retrospective analysis for Research and Applications, version 2 (MERRA-2)[116]

The near-surface air temperature data are obtained as monthly averages over 1980–2021 for all four reanalyses. Averaging is carried out in the same way as for the CMIP6 model data (see 'Surface temperature' section). The values for each reanalysis are shown by the solid black markers on Figs. 1a and 3a, and Supplementary Figs. 1, 5, and 6. Note that in these figures, the horizontal position of the ice-edge observations is the mean value of ΔT for the reanalyses. Likewise, the vertical position of the surface temperature changes from reanalyses is the mean of the lower and upper ice edge latitude change estimates.

Fig. 7 | Ocean parameters derived for the energy-balance model equation for the near-future period. a Change in poleward atmospheric heat transport, ΔAHT, plotted against that of ocean heat transport, ΔOHT, evaluated at 65°N. Each point is a difference in means over the two 21-year periods 1980–2000 and 2030–2050, for each combined historical and SSP3-7.0 simulation of the CMIP6 models listed in Table 1 (see also the legend of Fig. 4). The slope of this data gives the Bjerknes compensation rate, b_c, used in the energy-balance model (EBM) equation, determined by orthogonal distance regression, shown by the black line and grey shading. The legend states the slope value and its standard error, as well as the correlation, r, of the data. **b** As in (**a**) but for the southern hemisphere (heat transports evaluated at 60°S). **c** Change in rate of ocean heat uptake, $\Delta\partial_t H$, over the same time periods, plotted against ΔOHT. The slope of this data, determined similarly, gives the parameter h defined in Eq. (5). **d** As in (**c**) but for the southern hemisphere.

We compute estimates of the change in OHT from the Estimating the Circulation and Climate of the Ocean (ECCO) ocean state estimate. This is an adjoint-based ocean state-estimate that is constrained by observations and conserves heat and momentum[117]. The specific data we use is a derived product[118], the global northward OHT as a function of latitude, using a previously published method[119] on the latest available release of ECCO. The data spans 1992–2019. For our two historical averaging periods, 12 years are thus missing from the start of the first time average over 1980–2000, and 2 years are missing from the end of the second time average over 2001–2021. For the latter, we assume that the missing two years do not substantially affect the average and just approximate the average over 2001–2021 as that over 2001–2019. Figure 8 shows the yearly OHT time series for 65°N and 60°S in black and indicates this second averaging period in the blue horizontal lines.

Firstly, we approximate the average over 1980–2000 as that over 1992–2000, shown by the solid-red horizontal lines in Fig. 8—the same approach as that for the second averaging period (blue solid lines). The difference between the red and blue horizontal lines is then our stated central estimate of ΔOHT:

$$\Delta\text{OHT}_{\text{ECCO}} = \overline{\text{OHT}_{\text{ECCO}}\,(2001-2019)} - \overline{\text{OHT}_{\text{ECCO}}\,(1992-2000)}, \tag{17}$$

where overlines indicate averaging over the year ranges in brackets. This corresponds to the horizontal positions of the vertical lines for sea ice observations plotted in Figs. 1b and 3b. We then calculate a surrounding uncertainty interval by estimating what OHT for the missing years of the first time-averaging period could plausibly be, by assuming they exhibit similar statistical properties to the data we do have. Specifically, we are missing 12 years (1980–1991): we assume that the mean μ and standard deviation σ of those 12 years is the same as the nearest 12 years of available data, which is 1992–2003. The pink-shaded regions in Fig. 8 indicate this for the 65°N and 60°S OHT time series. We define an upper-bound average for 1980–2000 based on the known OHT data for 1992–2000 and using OHT = $\mu + \sigma$ (top edge of the pink shaded regions in Fig. 8) for each year in the range 1980–1991. A lower bound is similarly defined, using OHT = $\mu - \sigma$ for each missing year. These estimated upper and lower bound 1980–2000 averages are shown by the red dashed lines in Fig. 8. Subtracting each bound from the 2001–2019 average gives the uncertainty
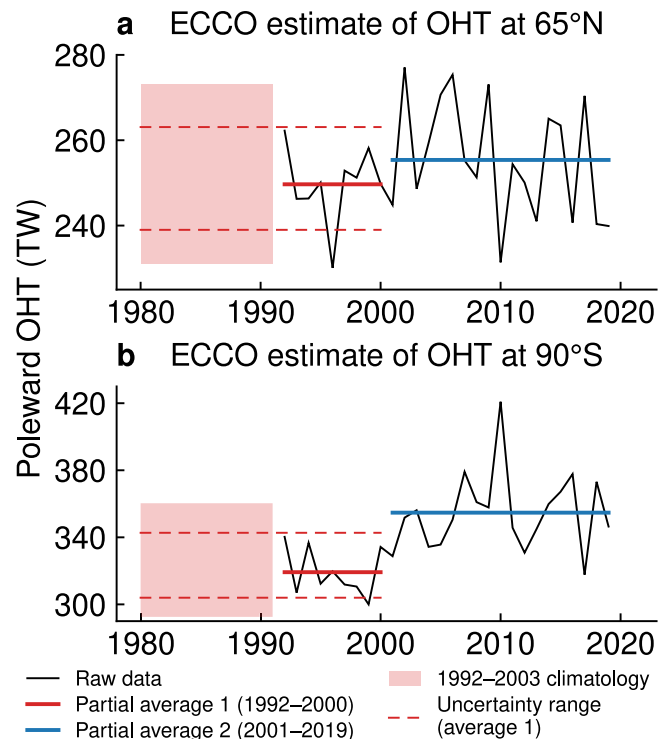

Fig. 8 | Estimating the change in ocean heat transports into the polar regions over the historical period 1980–2021. Poleward ocean heat transport (OHT; in units of 1 TW = 10^{12} W), annual-mean time series (black) evaluated at (**a**) 65°N and (**b**) 60°S using data from the Estimating the Circulation and Climate of the Ocean (ECCO) ocean state estimate. Data is only available from 1992–2019. Blue lines correspond to the average over 2001–2019, which partially corresponds to the second time averaging period in the historical analysis. Solid red lines correspond to the average over 1992–2000, which is roughly half of the required first-time averaging period 1980–2000. We estimate a likely range of 1980–2000 averages by assuming the missing data has the same climatology (mean and standard deviation) as the nearest available period of the same length, i.e., years 1992–2003, plotted as the pink-shaded regions. The red dashed lines are our lower and upper bounds on the average over 1980–2000 constructed from the combination of data for known years 1992–2000 and the upper and lower limits of the assumed climatology for 1980–1991.

interval:

$$\left[\overline{\text{OHT}_{\text{ECCO}}(2001 - 2019)} - (\mu \mp \sigma) \right], \tag{18}$$

corresponding to the width of the horizontal bars on Figs. 1b and 3b. Extrapolation of missing data is undesirable, even if the underlying assumptions are reasonable, so this approach gives us a central estimate of ΔOHT that is purely based on data, and shifts all such assumptions into a surrounding uncertainty interval. More traditional approaches would be to assume a continuation of trend over missing years: however, there is no clear (linear) trend in either time series, especially for the Arctic. Our resulting uncertainty interval using the approach described above includes ΔOHT = 0 for the Arctic (Fig. 1b).

Data availability
Raw CMIP6 model output is available from the Earth System Grid Federation (ESGF) data nodes. Atmospheric reanalysis model output data are available from the National Center for Atmospheric Research (NCAR) Research Data Archive (RDA; providing CFSR/CFSv2[120,121] and JRA-55[122]), the Copernicus Climate Data Store (CDS; ERA5[123]), and the Goddard Earth Sciences Data and Information Services Center (GES DISC; MERRA-2[124]). Sea ice concentration observation products are accessible from the NSIDC[125,126]. The ECCO ocean heat transport model output data is from version 4 release 5, release candidate 2, available online[118]. The processed CMIP6, atmospheric reanalyses, and passive-microwave sea ice-edge latitude diagnostics are deposited in the University of Reading Research Data Archive[127]. All aforementioned datasets are freely and publicly accessible.

Code availability
The code used to calculate all diagnostics from CMIP6 data, atmospheric reanalyses, and passive microwave data, is freely and publicly available online[128]. This includes scripts that, along with the archived data[127], reproduce all figures in the manuscript and supplementary information. The sea ice-edge latitude diagnostic code is available as a separate software package[104].

References
1. Christensen, M. & Nilsson, A. E. Arctic sea ice and the communication of climate change. *Pop. Commun.* **15**, 249–268 (2017).
2. Stroeve, J. & Notz, D. Changing state of Arctic sea ice across all seasons. *Environ. Res. Lett.* **13**, 103001 (2018).
3. Ho, J. The implications of Arctic sea ice decline on shipping. *Mar. Policy* **34**, 713–715 (2010).
4. Melia, N., Haines, K. & Hawkins, E. Sea ice decline and 21st century trans-Arctic shipping routes. *Geophys. Res. Lett.* **43**, 9720–9728 (2016).
5. Askenov, Y. et al. On the future navigability of Arctic sea routes: high-resolution projections of the Arctic Ocean and sea ice. *Mar. Policy* **75**, 300–317 (2017).
6. Macias-Fauria, M. & Post, E. Effects of sea ice on Arctic biota: an emerging crisis discipline. *Biol. Lett.* **14**, 20170702 (2018).
7. Huntington, H. P., Zagorsky, A. & Kaltenborn, B. P. et al. Societal implications of a changing Arctic Ocean. *Ambio* **51**, 298–306 (2022).
8. SIMIP Community. Arctic sea ice in CMIP6. *Geophys. Res. Lett.* **47**, e2019GL086749 (2020).
9. Screen, J. A. Far-flung effects of Arctic warming. *Nat. Geosci.* **10**, 253–254 (2017).
10. England, M. R., Polvani, L. M., Sun, L. & Deser, C. Tropical climate responses to projected Arctic and Antarctic sea-ice loss. *Nat. Geosci.* **13**, 275–281 (2020).
11. Flanner, M. G., Shell, K. M., Barlage, M., Perovich, D. K. & Tschudi, M. A. Radiative forcing and albedo feedback from the Northern Hemisphere cryosphere between 1979 and 2008. *Nat. Geosci.* **4**, 151–155 (2011).
12. Flocco, D., Schroeder, D., Feltham, D. L. & Hunke, E. C. Impact of melt ponds on Arctic sea ice simulations from 1990 to 2007. *J. Geophys. Res.* **117**, C09032 (2012).
13. Screen, J. A. & Simmonds, I. The central role of diminishing sea ice in recent Arctic temperature amplification. *Nature* **464**, 1334–1337 (2010).
14. Thackeray, C. W. & Hall, A. An emergent constraint on future Arctic sea-ice albedo feedback. *Nat. Clim. Change* **9**, 972–978 (2019).
15. Yumashev, D. et al. Climate policy implications of nonlinear decline of Arctic land permafrost and other cryosphere elements. *Nat. Commun.* **10**, https://doi.org/10.1038/s41467-019-09863-x (2019).
16. Parkinson, C. L. A 40-y record reveals gradual Antarctic sea ice increases followed by decreases at rates far exceeding the rates seen in the Arctic. *Proc. Natl. Acad. Sci.* **116**, 14414–14423 (2019).
17. Roach, L. A. et al. Antarctic sea ice area in CMIP6. *Geophys. Res. Lett.* **47**, e2019GL086729 (2020).
18. Stroeve, J. et al. Trends in Arctic sea ice extent from CMIP5, CMIP3 and observations. *Geophys. Res. Lett.* **39**, L16502 (2012).
19. Massonnet, F. et al. Constraining projections of summer Arctic sea ice. *Cryosphere* **6**, 1383–1394 (2012).
20. Turner, J., Bracegirdle, T. J., Phillips, T., Marshall, G. J. & Hosking, J. S. An initial assessment of Antarctic sea ice extent in CMIP5 models. *J. Clim.* **26**, 1473–1484 (2013).
21. Marzocchi, A. & Jansen, M. F. Connecting Antarctic sea ice to deep-ocean circulation in modern and glacial climate simulations. *Geophys. Res. Lett.* **44**, 6286–6295 (2017).
22. Shu, Q. et al. Assessment of sea ice extent in CMIP6 with comparison to observations and CMIP5. *Geophys. Res. Lett.* **47**, e2020GL087965 (2020).
23. Shen, Z., Duan, A., Li, D. & Li, J. Assessment and ranking of climate models in Arctic sea ice cover simulation: from CMIP5 to CMIP6. *J. Clim.* **34**, 3609–3627 (2021).
24. IPCC. Climate change 2021: the physical science basis. Contribution of Working Group I to the Sixth Assessment Report of the Intergovernmental Panel on Climate Change. In Masson-Delmotte, V. et al. (eds.) Technical Summary, 33–144 (Cambridge University Press, 2021). https://doi.org/10.1017/9781009157896.002.
25. Rosenblum, E. & Eisenman, I. Sea ice trends in climate models only accurate in runs with biased global warming. *J. Clim.* **30**, 6265–6278 (2017).
26. Notz, D. et al. The CMIP6 sea-ice model intercomparison project (SIMIP): understanding sea ice through climate-model simulations. *Geosci. Model Dev.* **9**, 3427–3446 (2016).
27. Goddard, L., Baethgen, W., Kirtman, B. & Meehl, G. The urgent need for improved climate models and predictions. *EOS Trans. AGU* **90**, 343 (2009).
28. Winton, M. On the climatic impact of ocean circulation. *J. Clim.* **16**, 2875–2889 (2003).
29. Bitz, C. M., Holland, M. M., Hunke, E. C. & Moritz, R. E. Maintenance of the sea-ice edge. *J. Clim.* **18**, 2903–2921 (2005).
30. Holland, M. M., Bitz, C. M. & Tremblay, B. Future abrupt reductions in the summer Arctic sea ice. *Geophys. Res. Lett.* **33**, L23503 (2006).
31. Koenigk, T. & Brodeau, L. Ocean heat transport into the Arctic in the twentieth and twenty-first century in EC-Earth. *Clim. Dyn.* **42**, 3101–3120 (2014).
32. Yeager, S. G., Karspeck, A. R. & Danabasoglu, G. Predicted slowdown in the rate of Atlantic sea ice loss. *Geophys. Res. Lett.* **42**, 10704–10713 (2015).
33. Singh, H. A., Rasch, P. J. & Rose, B. E. J. Increased ocean heat convergence into the high latitudes with CO$_2$ doubling enhances polar-amplified warming. *Geophys. Res. Lett.* **44**, 10583–10591 (2017).

34. Singh, H. A., Garuba, O. A. & Rasch, P. J. How asymmetries between Arctic and Antarctic climate sensitivity are modified by the ocean. *Geophys. Res. Lett.* **45**, 13031–13040 (2018).

35. Auclair, G. & Tremblay, L. B. The role of ocean heat transport in rapid sea ice declines of the Community Earth System Model Large Ensemble. *J. Geophys. Res.* **123**, 8941–8957 (2018).

36. Docquier, D., Koenigk, T., Fuentes-Franco, R., Karami, M. P. & Ruprich-Robert, Y. Impact of ocean heat transport on the Arctic sea-ice decline: a model study with EC-Earth3. *Clim. Dyn.* **56**, 1407–1432 (2021).

37. Docquier, D. & Koenigk, T. A review of interactions between ocean heat transport and Arctic sea ice. *Environ. Res. Lett.* **16**, 123002 (2021).

38. Decuypère, M., Tremblay, L. B. & Dufour, C. O. Impact of ocean heat transport on Arctic sea ice variability in the GFDL CM2-O suite. *J. Geophys. Res.* **127**, e2021JC017762 (2022).

39. Årthun, M., Eldevik, T., Smedsrud, L. H., Skagseth, Ø. & Ingvaldsen, R. B. Quantifying the influence of Atlantic heat on Barents sea ice variability and retreat. *J. Clim.* **25**, 4736–4743 (2012).

40. Polyakov, I. V. et al. Greater role for Atlantic inflows on sea-ice loss in the Eurasian Basin of the Arctic Ocean. *Science* **356**, 285–291 (2017).

41. Zhang, J. Increasing Antarctic sea ice under warming atmospheric and oceanic conditions. *J. Clim.* **20**, 2515–2529 (2007).

42. Goosse, H. & Zunz, V. Decadal trends in Antarctic sea ice extent ultimately controlled by ice–ocean feedback. *Cryosphere* **8**, 453–470 (2014).

43. Zhang, L., Delworth, T. L., Cooke, W. & Yang, X. Natural variability of Southern Ocean convection as a driver of observed climate trends. *Nat. Clim. Chang.* **9**, 59–65 (2019).

44. Mahlstein, I. & Knutti, R. Ocean heat transport as a cause for model uncertainty in projected Arctic warming. *J. Clim.* **24**, 1451–1460 (2011).

45. Nummelin, A., Li, C. & Hezel, P. J. Connecting ocean heat transport changes from the midlatitudes to the Arctic Ocean. *Geophys. Res. Lett.* **44**, 1899–1908 (2017).

46. Aylmer, J. R., Ferreira, D. & Feltham, D. L. Different mechanisms of Arctic and Antarctic sea ice response to ocean heat transport. *Clim. Dyn.* **59**, 315–329 (2022).

47. Pan, R. et al. Future Arctic climate change in CMIP6 strikingly intensified by NEMO-family climate models. *Geophys. Res. Lett.* **50**, e2022GL102077 (2023).

48. Lee, Y. J., Watts, M., Maslowski, W., Kinney, J. C. & Osinski, R. Assessment of the pan-Arctic accelerated rate of sea ice decline in CMIP6 historical simulations. *J. Clim.* **36**, 6069–6089 (2023).

49. Notz, D. & Stroeve, J. Observed Arctic sea-ice loss directly follows anthropogenic CO_2 emission. *Science* **354**, 747–750 (2016).

50. Burgard, C. & Notz, D. Drivers of Arctic Ocean warming in CMIP5 models. *Geophys. Res. Lett.* **44**, 4263–4271 (2017).

51. Budyko, M. I. The effect of solar radiation variations on the climate of the Earth. *Tellus* **21**, 611–619 (1969).

52. Sellers, W. D. A global climatic model based on the energy balance of the Earth–atmosphere system. *J. Appl. Meteorol. Climatol.* **8**, 392–400 (1969).

53. Held, I. M. & Suarez, M. J. Simple albedo feedback models of the icecaps. *Tellus* **26**, 613–629 (1974).

54. North, G. R., Cahalan, R. F. & Coakley Jr., J. A. Energy balance climate models. *Rev. Geophys.* **19**, 91–121 (1981).

55. North, G. R. The small ice cap instability in diffusive climate models. *J. Atmos. Sci.* **41**, 3390–3395 (1984).

56. Eisenman, I. & Wettlaufer, J. S. Nonlinear threshold behavior during the loss of Arctic sea ice. *Proc. Natl. Acad. Sci.* **106**, 28–32 (2009).

57. Rose, B. E. J. & Marshall, J. Ocean heat transport, sea ice, and multiple climate states: insights from energy balance models. *J. Atmos. Sci.* **66**, 2828–2843 (2009).

58. Ferreira, D., Marshall, J. & Rose, B. Climate determinism revisited: multiple equilibria in a complex climate model. *J. Climate* **24**, 992–1012 (2011).

59. Eisenman, I. Factors controlling the bifurcation structure of sea ice retreat. *J. Geophys. Res.* **117**, D01111 (2012).

60. Rose, B. E. J. Stable "Waterbelt" climates controlled by tropical ocean heat transport: a nonlinear coupled climate mechanism of relevance to Snowball Earth. *J. Geophys. Res.* **120**, 1404–1423 (2015).

61. Wagner, T. J. W. & Eisenman, I. How climate model complexity influences sea ice stability. *J. Clim.* **28**, 3998–4014 (2015).

62. Aylmer, J., Ferreira, D. & Feltham, D. Impacts of oceanic and atmospheric heat transports on sea ice extent. *J. Clim.* **33**, 7197–7215 (2020).

63. Roach, L. A., Eisenman, I., Wagner, T. J. W., Blanchard-Wrigglesworth, E. & Bitz, C. M. Asymmetry in the seasonal cycle of Antarctic sea ice driven by insolation. *Nat. Geosci.* **15**, 277–281 (2022).

64. England, M. R., Eisenman, I. & Wagner, T. J. W. Spurious climate impacts in coupled sea ice loss simulations. *J. Clim.* **35**, 7401–7411 (2022).

65. Hwang, Y.-T. & Frierson, D. M. W. Increasing atmospheric poleward energy transport with global warming. *Geophys. Res. Lett.* **37**, L24807 (2010).

66. Roe, G. H., Feldl, N., Armour, K. C., Hwang, Y.-T. & Frierson, D. M. W. The remote impacts of climate feedbacks on regional climate predictability. *Nat. Geosci.* **8**, 135–139 (2015).

67. Liu, Z., Yang, H., He, C. & Zhao, Y. A theory for Bjerknes compensation: the role of climate feedback. *J. Climate* **29**, 191–208 (2016).

68. Liu, Z., He, C. & Lu, F. Local and remote responses of atmospheric and oceanic heat transports to climate forcing: compensation versus collaboration. *J. Climate* **31**, 6445–6460 (2018).

69. Bonan, D. B., Armour, K. C., Roe, G. H., Siler, N. & Feldl, N. Sources of uncertainty in the meridional pattern of climate change. *Geophys. Res. Lett.* **45**, 9131–9140 (2018).

70. Siler, N., Roe, G. H. & Armour, K. C. Insights into the zonal-mean response of the hydrologic cycle to global warming from a diffusive energy balance model. *J. Clim.* **31**, 7481–7493 (2018).

71. Armour, K. C., Siler, N., Donohoe, A. & Roe, G. H. Meridional atmospheric heat transport constrained by energetics and mediated by large-scale diffusion. *J. Clim.* **32**, 3655–3680 (2019).

72. Hill, S. A., Burls, N. J., Fedorov, A. & Merlis, T. M. Symmetric and antisymmetric components of polar-amplified warming. *J. Clim.* **35**, 6757–6772 (2022).

73. Bonan, D. B., Siler, N., Roe, G. H. & Armour, K. C. Energetic constraints on the pattern of changes to the hydrological cycle under global warming. *J. Clim.* **36**, 3499–3522 (2023).

74. Mauritsen, T. et al. Tuning the climate of a global model. *J. Adv. Model. Earth Syst.* **4**, M00A01 (2012).

75. Notz, D. How well must climate models agree with observations? *Philos. Trans. R. Soc. A* **373**, 20140164 (2015).

76. Hourdin, F. et al. The art and science of climate model tuning. *Bull. Am. Meteorol. Soc.* **98**, 589–602 (2017).

77. Koll, D. D. B. & Cronin, T. W. Earth's outgoing longwave radiation linear due to H_2O greenhouse effect. *Proc. Natl. Acad. Sci.* **115**, 10293–10298 (2018).

78. Zhang, Y., Jeevanjee, N. & Fueglistaler, S. Linearity of outgoing longwave radiation: from an atmospheric column to global climate models. *Geophys. Res. Lett.* **47**, e2020GL089235 (2020).

79. Bjerknes, J. Atlantic air–sea interaction. *Adv. Geophys.* **10**, 1–82 (1964).

80. Shaffrey, L. & Sutton, R. Bjerknes compensation and the decadal variability of the energy transports in a coupled climate model. *J. Clim.* **19**, 1167–1181 (2006).

81. Outten, S. & Esau, I. Bjerknes compensation in the Bergen climate model. *Clim. Dyn.* **49**, 2249–2260 (2017).

82. Outten, S., Esau, I. & Ottera&ring, O. H. Bjerknes compensation in the CMIP5 climate models. *J. Clim.* **31**, 8745–8760 (2018).

83. Liu, Y., Attema, J. & Hazeleger, W. Atmosphere–ocean interactions and their footprint on heat transport variability in the northern hemisphere. *J. Clim.* **33**, 3691–3710 (2020).

84. Li, S. & Liu, W. Impacts of Arctic sea ice loss on global ocean circulations and interbasin ocean heat exchanges. *Clim. Dyn.* **59**, 2701–2716 (2022).

85. Docquier, D., Vannitsem, S., Ragone, F., Wyser, K. & Liang, X. S. Causal links between Arctic sea ice and its potential drivers based on the rate of information transfer. *Geophys. Res. Lett.* **49**, e2021GL095892 (2022).

86. Swart, N. C., Fyfe, J. C., Hawkins, E., Kay, J. E. & Jahn, A. Influence of internal variability on Arctic sea-ice trends. *Nat. Clim. Change* **5**, 86–89 (2015).

87. Bonan, D. B., Lehner, F. & Holland, M. M. Partitioning uncertainty in projections of Arctic sea ice. *Environ. Res. Lett.* **16**, 044002 (2021).

88. Notz, D. & Stroeve, J. The trajectory towards a seasonally ice-free Arctic Ocean. *Curr. Clim. Chang. Rep.* **4**, 407–416 (2018).

89. Årthun, M., Onarheim, I. H., Dörr, J. & Eldevik, T. The seasonal and regional transition to an ice-free Arctic. *Geophys. Res. Lett.* **48**, e2020GL090825 (2021).

90. Bonan, D. B., Schneider, T., Eisenman, I. & Wills, R. C. J. Constraining the date of a seasonally ice-free Arctic using a simple model. *Geophys. Res. Lett.* **48**, e2021GL094309 (2021).

91. Diebold, F. X. & Rudebusch, G. D. Probability assessments of an ice-free Arctic: comparing statistical and climate model projections. *J. Econom.* **231**, 520–534 (2022).

92. Kim, Y.-H., Min, S.-K., Gillett, N. P., Notz, D. & Malinina, E. Observationally-constrained projections of an ice-free Arctic even under a low emission scenario. *Nat. Commun.* **14**, 3139 (2023).

93. Topál, D. & Ding, Q. Atmospheric circulation-constrained model sensitivity recalibrates Arctic climate projections. *Nat. Clim. Chang.* **13**, 710–718 (2023).

94. Rainville, L. & Woodgate, R. A. Observations of internal wave generation in the seasonally ice-free Arctic. *Geophys. Res. Lett.* **36**, L23604 (2009).

95. Day, J. J., Bamber, J. L., Valdes, P. J. & Kohler, J. The impact of a seasonally ice free Arctic Ocean on the temperature, precipitation and surface mass balance of Svalbard. *Cryosphere* **6**, 35–50 (2012).

96. Day, J. J., Bamber, J. L. & Valdes, P. J. The Greenland Ice Sheet's surface mass balance in a seasonally sea ice-free Arctic. *J. Geophys. Res.* **118**, 1533–1544 (2013).

97. Liu, J. et al. Arctic sea-ice loss is projected to lead to more frequent strong El Niño events. *Nat. Commun.* **13**, 4952 (2022).

98. Aylmer, J. R. Ocean Heat Transport and the Latitude of the Sea Ice Edge. Ph.D. Thesis, https://doi.org/10.48683/1926.00108418 (University of Reading, 2022).

99. Hahn, L. C., Armour, K. C., Battisti, D. S., Donohoe, A. G. & Bitz, C. M. Antarctic elevation drives hemispheric asymmetry in polar lapse rate climatology and feedback. *Geophys. Res. Lett.* **47**, e2020GL088965 (2020).

100. Frey, W. R., Morrison, A. L., Kay, J. E., Guzman, R. & Chepfer, H. The combined influence of observed Southern Ocean clouds and sea ice on top-of-atmosphere albedo. *J. Geophys. Res.* **123**, 4461–4475 (2018).

101. Eyring, V. et al. Overview of the Coupled Model Intercomparison Project Phase 6 (CMIP6) experimental design and organization. *Geosci. Model Dev.* **9**, 1937–1958 (2016).

102. O'Neill, B. C. et al. The Scenario Model Intercomparison Project (ScenarioMIP) for CMIP6. *Geosci. Model Dev.* **9**, 3461–3482 (2016).

103. Eisenman, I. Geographic muting of changes in the Arctic sea ice cover. *Geophys. Res. Lett.* **37**, L16501 (2010).

104. Aylmer, J. R. Sea ice-edge latitude diagnostic code, version 1.0.0. Zenodo. https://doi.org/10.5281/zenodo.5494524 (2021).

105. Griffies, S. M. et al. OMIP contribution to CMIP6: experimental and diagnostic protocol for the physical component of the Ocean Model Intercomparison Project. *Geosci. Model Dev.* **9**, 3231–3296 (2016).

106. Voldoire, A. et al. Evaluation of CMIP6 DECK experiments with CNRM-CM6-1. *J. Adv. Model. Earth Syst.* **11**, 2177–2213 (2019).

107. Séférian, R. et al. Evaluation of CNRM Earth System Model, CNRM-ESM2-1: role of Earth system processes in present-day and future climate. *J. Adv. Model. Earth Syst.* **11**, 4182–4227 (2019).

108. Sellar, A. A. et al. UKESM1: description and evaluation of the U.K. Earth System Model. *J. Adv. Model. Earth Syst.* **11**, 4513–4558 (2019).

109. Juckes, M. et al. The CMIP6 Data Request (DREQ, version 01.00.31). *Geosci. Model Dev.* **13**, 201–224 (2020).

110. Draper, N. R. & Smith, H. Applied Regression Analysis, 3 edn (John Wiley, 1998).

111. Comiso, J. C., Cavalieri, D. J., Parkinson, C. L. & Gloersen, P. Passive microwave algorithms for sea ice concentration: a comparison of two techniques. *Remote Sens. Environ.* **60**, 357–384 (1997).

112. Saha, S. et al. The NCEP climate forecast system reanalysis. *Bull. Am. Meteorol. Soc.* **91**, 1015–1058 (2010).

113. Saha, S. et al. The NCEP Climate Forecast System Version 2. *J. Clim.* **27**, 2185–2208 (2014).

114. Hersbach, H. et al. The ERA5 global reanalysis. *Q. J. R. Meteorol. Soc.* **146**, 1999–2049 (2020).

115. Kobayashi, S. et al. The JRA-55 reanalysis: general specifications and basic characteristics. *J. Meteorol. Soc. Jpn* **93**, 5–48 (2015).

116. Gelaro, R. et al. The modern-era retrospective analysis for research and applications, version 2 (MERRA2). *J. Clim.* **30**, 5419–5454 (2017).

117. Forget, G. et al. ECCO version 4: an integrated framework for non-linear inverse modeling and global ocean state estimation. *Geosci. Model Dev.* **8**, 3071–3104 (2015).

118. Forget, G. ECCO v4 standard analysis sample (v4r5-rc2) [Data set]. Zenodo. https://doi.org/10.5281/zenodo.7869067 (2023).

119. Forget, G. & Ferreira, D. Global ocean heat transport dominated by heat export from the tropical Pacific. *Nat. Geosci.* **12**, 351–354 (2019).

120. Saha, S. et al. NCEP Climate Forecast System Reanalysis (CFSR) monthly products, January 1979 to December 2010, accessed 23 February 2024; https://doi.org/10.5065/D6DN438J (2010).

121. Saha, S. et al. NCEP Climate Forecast System Version 2 (CFSv2) monthly products. Research Data Archive at the National Center for Atmospheric Research, Computational and Information Systems Laboratory, Boulder, CO, accessed 23 February 2024; https://doi.org/10.5065/D69021ZF (2012).

122. Japan Meteorological Agency/Japan. JRA-55: Japanese 55-year reanalysis, monthly means and variances. Research Data Archive at the National Center for Atmospheric Research, Computational and Information Systems Laboratory, Boulder, CO, accessed 23 February 2024; https://doi.org/10.5065/D60G3H5B (2013).

123. Hersbach, H. et al. ERA5 monthly averaged data on single levels from 1940 to present. Copernicus Climate Change Service (C3S) Climate Data Store (CDS), accessed 23 February 2024; https://doi.org/10.24381/cds.f17050d7 (2023).

124. Global Modeling and Assimilation Office (GMAO). MERRA-2 instM_2d_asm_Nx: 2d, Monthly mean, Single-Level, Assimilation, Single-Level Diagnostics v5.12.4. Goddard Earth Sciences Data and Information Services Center (GES DISC), Greenbelt, MD, USA, accessed 23 February 2024; https://doi.org/10.5067/5ESKGQTZG7FO (2015).

125. DiGirolamo, N., Parkinson, C. L., Cavalieri, D. J., Gloersen, P. & Zwally, H. J. Sea ice concentrations from Nimbus-7 SMMR and DMSP SSM/I-SSMIS passive microwave data, version 2. NASA

National Snow and Ice Data Center Distributed Active Archive Center, accessed 15 April 2024; https://doi.org/10.5067/MPYG15WAA4WX (2022).

126. Comiso, J. C. Bootstrap sea ice concentrations from Nimbus-7 SMMR and DMSP SSM/I-SSMIS passive microwave data, version 4. NASA National Snow and Ice Data Center Distributed Active Archive Center, accessed 15 April 2024; https://doi.org/10.5067/X5LG68MH013O (2023).

127. Aylmer, J. R. Diagnostics from CMIP6, atmospheric reanalyses, and passive-microwave observations used to examine the impact of ocean heat transport on Arctic and Antarctic sea ice. University of Reading. https://doi.org/10.17864/1947.001333 (2024).

128. Aylmer, J. R. CMIP6 data processing code for examination of the impact of ocean heat transport on Arctic and Antarctic sea ice, version 1.0.0. Zenodo. https://doi.org/10.5281/zenodo.12207486 (2024).

129. Semmler, T. et al. Simulations for CMIP6 with the AWI Climate Model AWI-CM-1-1. *J. Adv. Model. Earth Syst.* **12**, e2019MS002009 (2020).

130. Semmler, T. et al. AWI AWI-CM-1.1-MR model output prepared for CMIP6 CMIP piControl, version 20191015. Earth System Grid Federation. https://doi.org/10.22033/ESGF/CMIP6.2777 (2018).

131. Semmler, T. et al. AWI AWI-CM-1.1-MR model output prepared for CMIP6 CMIP historical, version 20200720. Earth System Grid Federation. https://doi.org/10.22033/ESGF/CMIP6.2686 (2018).

132. Semmler, T. et al. AWI AWI-CM-1.1-MR model output prepared for CMIP6 ScenarioMIP ssp370, version 20190529. Earth System Grid Federation. https://doi.org/10.22033/ESGF/CMIP6.2803 (2019).

133. Danabasoglu, G. et al. The Community Earth System Model version 2 (CESM2). *J. Adv. Model. Earth Syst.* **12**, e2019MS001916 (2020).

134. Danabasoglu, G., Lawrence, D., Lindsay, K., Lipscomb, W. & Strand, G. NCAR CESM2 model output prepared for CMIP6 CMIP piControl, version 20190320. Earth System Grid Federation. https://doi.org/10.22033/ESGF/CMIP6.7733 (2019).

135. Danabasoglu, G. NCAR CESM2 model output prepared for CMIP6 CMIP historical, version 20190308. Earth System Grid Federation. https://doi.org/10.22033/ESGF/CMIP6.7627 (2019).

136. Danabasoglu, G. NCAR CESM2 model output prepared for CMIP6 ScenarioMIP ssp370, version 20200528. Earth System Grid Federation. https://doi.org/10.22033/ESGF/CMIP6.7753 (2019).

137. Danabasoglu, G. NCAR CESM2-FV2 model output prepared for CMIP6 CMIP piControl, version 20220915. Earth System Grid Federation. https://doi.org/10.22033/ESGF/CMIP6.11301 (2019).

138. Danabasoglu, G. NCAR CESM2-FV2 model output prepared for CMIP6 CMIP historical, version 20220915. Earth System Grid Federation. https://doi.org/10.22033/ESGF/CMIP6.11297 (2019).

139. Danabasoglu, G. NCAR CESM2-FV2 model output prepared for CMIP6 ScenarioMIP ssp370, version 20220915. Earth System Grid Federation. http://cera-www.dkrz.de/WDCC/meta/CMIP6/CMIP6.ScenarioMIP.NCAR.CESM2-FV2.ssp370 (2023).

140. Danabasoglu, G. NCAR CESM2-WACCM model output prepared for CMIP6 CMIP piControl, version 20190320. Earth System Grid Federation. https://doi.org/10.22033/ESGF/CMIP6.10094 (2019).

141. Danabasoglu, G. NCAR CESM2-WACCM model output prepared for CMIP6 CMIP historical, version 20190227. Earth System Grid Federation. https://doi.org/10.22033/ESGF/CMIP6.10071 (2019).

142. Danabasoglu, G. NCAR CESM2-WACCM model output prepared for CMIP6 ScenarioMIP ssp370, version 20190815. Earth System Grid Federation. https://doi.org/10.22033/ESGF/CMIP6.10102 (2019).

143. Voldoire, A. CNRM-CERFACS CNRM-CM6-1 model output prepared for CMIP6 CMIP historical, version 20180917. Earth System Grid Federation. https://doi.org/10.22033/ESGF/CMIP6.4066 (2018).

144. Voldoire, A. CNRM-CERFACS CNRM-CM6-1 model output prepared for CMIP6 ScenarioMIP ssp370, version 20190219. Earth System Grid Federation. https://doi.org/10.22033/ESGF/CMIP6.4197 (2019).

145. Voldoire, A. CNRM-CERFACS CNRM-CM6-1-HR model output prepared for CMIP6 CMIP piControl, version 20191021. Earth System Grid Federation. https://doi.org/10.22033/ESGF/CMIP6.4164 (2019).

146. Voldoire, A. CNRM-CERFACS CNRM-CM6-1-HR model output prepared for CMIP6 CMIP historical, version 20191021. Earth System Grid Federation. https://doi.org/10.22033/ESGF/CMIP6.4067 (2019).

147. Voldoire, A. CNRM-CERFACS CNRM-CM6-1-HR model output prepared for CMIP6 ScenarioMIP ssp370, version 20200127. Earth System Grid Federation. https://doi.org/10.22033/ESGF/CMIP6.4198 (2020).

148. Séférian, R. CNRM-CERFACS CNRM-ESM2-1 model output prepared for CMIP6 CMIP historical, version 20181206. Earth System Grid Federation. https://doi.org/10.22033/ESGF/CMIP6.4068 (2018).

149. Voldoire, A. CNRM-CERFACS CNRM-ESM2-1 model output prepared for CMIP6 ScenarioMIP ssp370, version 20191021. Earth System Grid Federation. https://doi.org/10.22033/ESGF/CMIP6.4199 (2019).

150. Swart, N. C. et al. The Canadian Earth System Model version 5 (CanESM5.0.3). *Geosci. Model Dev.* **12**, 4823–4873 (2019).

151. Swart, N. C. et al. CCCma CanESM5 model output prepared for CMIP6 CMIP piControl, version 20190429. Earth System Grid Federation. https://doi.org/10.22033/ESGF/CMIP6.3673 (2019).

152. Swart, N. C. et al. CCCma CanESM5 model output prepared for CMIP6 CMIP historical, version 20190429. Earth System Grid Federation. https://doi.org/10.22033/ESGF/CMIP6.3610 (2019).

153. Swart, N. C. et al. CCCma CanESM5 model output prepared for CMIP6 ScenarioMIP ssp370, version 20190429. Earth System Grid Federation. https://doi.org/10.22033/ESGF/CMIP6.3690 (2019).

154. Swart, N. C. et al. CCCma CanESM5-CanOE model output prepared for CMIP6 CMIP piControl, version 20190429. Earth System Grid Federation. https://doi.org/10.22033/ESGF/CMIP6.10266 (2019).

155. Swart, N. C. et al. CCCma CanESM5-CanOE model output prepared for CMIP6 CMIP historical, version 20190429. Earth System Grid Federation. https://doi.org/10.22033/ESGF/CMIP6.10260 (2019).

156. Swart, N. C. et al. CCCma CanESM5-CanOE model output prepared for CMIP6 ScenarioMIP ssp370, version 20190429. Earth System Grid Federation. https://doi.org/10.22033/ESGF/CMIP6.10271 (2019).

157. Dunne, J. P. et al. The GFDL Earth System Model version 4.1 (GFDL-ESM 4.1): overall coupled model description and simulation characteristics. *J. Adv. Model. Earth Syst.* **12**, e2019MS002015 (2020).

158. Krasting, J. P. et al. NOAA-GFDL GFDL-ESM4 model output prepared for CMIP6 CMIP piControl, version 20180701. Earth System Grid Federation. https://doi.org/10.22033/ESGF/CMIP6.8669 (2018).

159. Krasting, J. P. et al. NOAA-GFDL GFDL-ESM4 model output prepared for CMIP6 CMIP historical, version 20190726. Earth System Grid Federation. https://doi.org/10.22033/ESGF/CMIP6.8597 (2018).

160. John, J. G. et al. NOAA-GFDL GFDL-ESM4 model output prepared for CMIP6 ScenarioMIP ssp370, version 20180701. Earth System Grid Federation. https://doi.org/10.22033/ESGF/CMIP6.8691 (2018).

161. Rind, D. et al. GISS model E2.2: a climate model optimized for the middle atmosphere—model structure, climatology, variability, and climate sensitivity. *J. Geophys. Res.* **125**, e2019JD032204 (2020).

162. NASA Goddard Institute for Space Studies (NASA/GISS). NASA-GISS GISS-E2-2-G model output prepared for CMIP6 CMIP piControl, version 20211002. Earth System Grid Federation. https://doi.org/10.22033/ESGF/CMIP6.7382 (2019).

163. NASA Goddard Institute for Space Studies (NASA/GISS). NASA-GISS GISS-E-2-2-G model output prepared for CMIP6 CMIP historical, version 20211020. Earth System Grid Federation. https://doi.org/10.22033/ESGF/CMIP6.7129 (2019).

164. NASA Goddard Institute for Space Studies (NASA/GISS). NASA-GISS GISS-E-2-2-G model output prepared for CMIP6 ScenarioMIP ssp370, version 20211015. Earth System Grid Federation. https://doi.org/10.22033/ESGF/CMIP6.11873 (2021).

165. Boucher, O. et al. Presentation and evaluation of the IPSL-CM6A-LR climate model. *J. Adv. Model. Earth Syst.* **12**, e2019MS002010 (2020).

166. Boucher, O. et al. IPSL IPSL-CM6A-LR model output prepared for CMIP6 CMIP piControl, version 20200326. Earth System Grid Federation. https://doi.org/10.22033/ESGF/CMIP6.5251 (2018).

167. Boucher, O. et al. IPSL IPSL-CM6A-LR model output prepared for CMIP6 CMIP historical, version 20180803. Earth System Grid Federation. https://doi.org/10.22033/ESGF/CMIP6.5195 (2018).

168. Boucher, O. et al. IPSL IPSL-CM6A-LR model output prepared for CMIP6 ScenarioMIP ssp370, version 20190119. Earth System Grid Federation. https://doi.org/10.22033/ESGF/CMIP6.5265 (2019).

169. Tatebe, H. et al. Description and basic evaluation of simulated mean state, internal variability, and climate sensitivity in MIROC6. *Geosci. Model Dev.* **12**, 2727–2765 (2019).

170. Tatebe, H. & Watanabe, M. MIROC MIROC6 model output prepared for CMIP6 CMIP piControl, version 20181212. Earth System Grid Federation. https://doi.org/10.22033/ESGF/CMIP6.5711 (2018).

171. Tatebe, H. & Watanabe, M. MIROC MIROC6 model output prepared for CMIP6 CMIP historical, version 20181212. Earth System Grid Federation. https://doi.org/10.22033/ESGF/CMIP6.5603 (2018).

172. Shiogama, H., Abe, M. & Tatebe, H. MIROC MIROC6 model output prepared for CMIP6 ScenarioMIP ssp370, version 20190627. Earth System Grid Federation. https://doi.org/10.22033/ESGF/CMIP6.5752 (2019).

173. Müller, W. A. et al. A higher-resolution version of the Max Planck Institute Earth System Model (MPI-ESM1.2-HR). *J. Adv. Model. Earth Syst.* **10**, 1383–1413 (2018).

174. Jungclaus, J. et al. MPI-M MPI-ESM1.2-HR model output prepared for CMIP6 CMIP piControl, version 20190710. Earth System Grid Federation. https://doi.org/10.22033/ESGF/CMIP6.6674 (2019).

175. Jungclaus, J. et al. MPI-M MPI-ESM1.2-HR model output prepared for CMIP6 CMIP historical, version 20190710. Earth System Grid Federation. https://doi.org/10.22033/ESGF/CMIP6.6594 (2019).

176. Schupfner, M. et al. DKRZ MPI-ESM1.2-HR model output prepared for CMIP6 ScenarioMIP ssp370, version 20190710. Earth System Grid Federation. https://doi.org/10.22033/ESGF/CMIP6.4399 (2019).

177. Mauritsen, T. et al. Developments in the MPI-M Earth System Model version 1.2 (MPI-ESM1.2) and its response to increasing CO_2. *J. Adv. Model. Earth Syst.* **11**, 998–1038 (2019).

178. Wieners, K.-H. et al. MPI-M MPI-ESM1.2-LR model output prepared for CMIP6 CMIP piControl, version 20190710. Earth System Grid Federation. https://doi.org/10.22033/ESGF/CMIP6.6675 (2019).

179. Wieners, K.-H. et al. MPI-M MPI-ESM1.2-LR model output prepared for CMIP6 CMIP historical, version 20190710. Earth System Grid Federation. https://doi.org/10.22033/ESGF/CMIP6.6595 (2019).

180. Wieners, K.-H. et al. MPI-M MPI-ESM1.2-LR model output prepared for CMIP6 ScenarioMIP ssp370, version 20190710. Earth System Grid Federation. https://doi.org/10.22033/ESGF/CMIP6.6695 (2019).

181. Yukimoto, S. et al. The Meteorological Research Institute Earth System Model version 2.0, MRI-ESM2.0: description and basic evaluation of the physical component. *J. Meteorol. Soc. Jpn* **97**, 931–965 (2019).

182. Yukimoto, S. et al. MRI MRI-ESM2.0 model output prepared for CMIP6 CMIP piControl, version 20190222. Earth System Grid Federation. https://doi.org/10.22033/ESGF/CMIP6.6900 (2019).

183. Yukimoto, S. et al. MRI MRI-ESM2.0 model output prepared for CMIP6 CMIP historical, version 20190222. Earth System Grid Federation. https://doi.org/10.22033/ESGF/CMIP6.6842 (2019).

184. Yukimoto, S. et al. MRI MRI-ESM2.0 model output prepared for CMIP6 ScenarioMIP ssp370, version 20190222. Earth System Grid Federation. https://doi.org/10.22033/ESGF/CMIP6.6915 (2019).

185. Seland, Ø. et al. Overview of the Norwegian Earth System Model (NorESM2) and key climate response of CMIP6 DECK, historical, and scenario simulations. *Geosci. Model Dev.* **13**, 6165–6200 (2020).

186. Seland, Ø. et al. NCC NorESM2-LM model output prepared for CMIP6 CMIP piControl, version 20210118. Earth System Grid Federation. https://doi.org/10.22033/ESGF/CMIP6.8217 (2019).

187. Seland, Ø. et al. NCC NorESM2-LM model output prepared for CMIP6 CMIP historical, version 20190815. Earth System Grid Federation. https://doi.org/10.22033/ESGF/CMIP6.8036 (2019).

188. Seland, Ø. et al. NCC NorESM2-LM model output prepared for CMIP6 ScenarioMIP ssp370, version 20191108. Earth System Grid Federation. https://doi.org/10.22033/ESGF/CMIP6.8268 (2019).

189. Bentsen, M. et al. NCC NorESM2-MM model output prepared for CMIP6 CMIP piControl, version 20191108. Earth System Grid Federation. https://doi.org/10.22033/ESGF/CMIP6.8221 (2019).

190. Bentsen, M. et al. NCC NorESM2-MM model output prepared for CMIP6 CMIP historical, version 20191108. Earth System Grid Federation. https://doi.org/10.22033/ESGF/CMIP6.8040 (2019).

191. Bentsen, M. et al. NCC NorESM2-MM model output prepared for CMIP6 ScenarioMIP ssp370, version 20191108. Earth System Grid Federation. https://doi.org/10.22033/ESGF/CMIP6.8270 (2019).

192. Tang, Y. et al. MOHC UKESM1.0-LL model output prepared for CMIP6 CMIP piControl, version 20200828. Earth System Grid Federation. https://doi.org/10.22033/ESGF/CMIP6.6298 (2019).

193. Tang, Y. et al. MOHC UKESM1.0-LL model output prepared for CMIP6 CMIP historical, version 20190406. Earth System Grid Federation. https://doi.org/10.22033/ESGF/CMIP6.6113 (2019).

194. Good, P. et al. MOHC UKESM1.0-LL model output prepared for CMIP6 ScenarioMIP ssp370, version 20190510. Earth System Grid Federation. https://doi.org/10.22033/ESGF/CMIP6.6347 (2019).

195. Mulcahy, J. et al. MOHC UKESM1.1-LL model output prepared for CMIP6 CMIP piControl, version 20220505. Earth System Grid Federation. https://doi.org/10.22033/ESGF/CMIP6.16823 (2022).

196. Mulcahy, J. et al. MOHC UKESM1.1-LL model output prepared for CMIP6 CMIP historical, version 20220512. Earth System Grid Federation. https://doi.org/10.22033/ESGF/CMIP6.16797 (2022).

197. Walton, J. et al. MOHC UKESM1.1-LL model output prepared for CMIP6 ScenarioMIP ssp370, version 20220512. Earth System Grid Federation. https://doi.org/10.22033/ESGF/CMIP6.16845 (2022).

Acknowledgements

Author contributions

Jake R. Aylmer processed and analysed the CMIP6 and observation data, derived the EBM equation and prepared the manuscript. David Ferreira and Daniel L. Feltham provided expert guidance and management of the wider

research project including feedback on the initial and subsequent drafts of this article. All authors contributed equally to the discussion and interpretation of results.